Large Scale Structure in the Lyman Alpha Forest

von

Jochen Liske

Diplomarbeit in Physik
angefertigt im
Department of Astrophysics and Optics
der
University of New South Wales
Sydney

vorgelegt der
Mathematisch-Naturwissenschaftlichen Fakultät
der
Rheinischen Friedrich-Wilhelms-Universität
Bonn

im April 1997

Referent	:	Prof. Dr. U. Mebold
Korreferent	:	Dr. J.K. Webb

Contents

Chapter 1

Introduction

1.1 Large scale structure and the Lyman-α forest

One of the major tasks of cosmology is to investigate and explain the nature of structure formation in the Universe. Any theory thereof must match the cosmological observations. At very high redshifts the models are constrained by observations of the cosmic microwave background (CMB) and at low redshifts the constraints come from the large scale distribution of galaxies. At intermediate redshifts, possibly the richest source of information on cosmological structure is the Lyman-α forest: a multitude of absorption lines observed in the spectra of high redshift quasars blueward of the Lyα emission line. Lynds (1971) was the first to discover these lines in the spectrum of 4C 05.34 and correctly attribute them to a large number of intervening hydrogen "clouds" — the Lyα absorbers. Quasars are the most distant and luminous objects known and each line of sight indiscriminately probes the distribution of the intervening neutral hydrogen out to redshifts of ~ 5 when the Universe was only 7 percent of its present age and one sixth of its present size. This provides us with an independent data set between the CMB at redshift ~ 1000 and the local distribution of galaxies at redshifts < 0.5.

After some initial controversy over whether the absorption occurred in gas emitted by the quasar itself or in intervening material, the Lyα absorbers were soon established as an *intergalactic* population which was not associated with galaxies (Sargent et al. 1980). This conclusion was based on three findings. Firstly, they seemed to contain no metals and could thus not have been exposed to star forming regions, i.e. galaxies. Secondly, their spatial distribution seemed to be completely random and unclustered, unlike what one would have expected for galaxies at these redshifts. Thirdly, the extremely large cross-section of absorbers as inferred from the number evolution with redshift seemed inconsistent with the sizes of galaxies.

Subsequent to this, high resolution spectroscopy has revealed a great deal of information about the statistical properties of the Lyα forest. Almost all of this information was gained by detailed fitting of the absorption lines with Voigt profiles. This procedure results in three parameters for each line: a position, expressed as redshift z, a column density N and a Doppler width b which in the case of purely thermal broadening is related to the cloud's temperature by $b = \sqrt{2kT/m}$. In particular, it was found that the distribution of absorption line parameters takes on the form of a power law as a function of redshift and column density and that the dependency on the Doppler width is approximately Gaussian (Carswell et al. 1984).

The clustering analyses were performed using the two-point correlation function (Sargent et al. 1980) which was measured in velocity space by constructing the histogram of velocity splittings of pairs of absorption lines[1]. Webb (1987) was the first to detect any correlation in the Lyα clouds and others were to follow (Rauch et al. 1992, Ulmer 1996). The clustering signal found by these investigators was generally weak and on too small a scale to convincingly dismiss the intergalactic hypothesis.

Since then however, it has been demonstrated (Fernández-Soto et al. 1996) that the blending of Lyα absorption lines due to finite spectral resolution and their intrinsic width may "hide" significant amounts of clustering. Fernández-Soto et al. attempted to sidestep this effect by using much narrower absorption lines

[1] In the rest of this work this procedure will generically be referred to as "line counting".

produced by CIV associated with some of the Lyα absorbers. As a result they found a strong clustering signal. In addition, it was argued earlier (Liu & Jones 1990) that some information on clustering of Lyα clouds, especially on large scales, may be lost in two-point correlation function analyses due to the effects of the finite size of the sample.

In contrast to Lyα clouds, *metal* absorption lines were found to cluster strongly at high redshift on scales similar to local superclusters (Williger et al. 1996, Quashnock et al. 1997) and these systems were associated with high redshift galaxies.

The advent of the Hubble Space Telescope (HST) made it possible to observe the Lyα forest at redshifts below ~ 2. This regime was not accessible before because of the poor atmospheric transmission in the ultraviolet wavelength region. Lanzetta et al. (1995) subsequently carried out a deep redshift survey of galaxies lying close (in the plane of the sky) to bright quasars which had been observed spectroscopically with HST's Faint Object Spectrograph. They found statistically significant coincidences between galaxy and Lyα absorber redshifts, implying that a significant fraction of Lyα absorbers are directly caused by gaseous envelopes around faint galaxies at redshifts $\sim 1/2$.

An equally important result arose from recent work by Cowie et al. (1995) using the Keck 10 m telescope. They obtained extremely high signal to noise ratio spectra of quasars, covering the spectral region below the CIV emission line. They found numerous weak CIV absorption systems associated with Lyα absorption lines *whose characteristics satisfy those historically associated with Lyα forest clouds.* In fact, Cowie et al. found that roughly half of all Lyα clouds with $N > 3 \times 10^{14}$ cm^{-2} contain measurable amounts of CIV.

Thus we now have evidence that Lyα absorbers *do* cluster, that they *do* contain metals, and that at low redshift some fraction may be identified with galaxies. Therefore, we may conjecture that high redshift Lyα absorbers are the extended haloes of galaxies or the progenitors thereof. In this case, Lyα absorbers are a good tracer of the baryonic matter distribution at high redshifts and may be useful in studying structure formation. In light of the past failure of the line counting technique in detecting large scale structure new methods must be devised. In this work I propose a new tool for analysing the Lyα forest in search of large scale structure. This method is applied successfully to a group of eight closely spaced quasars. In the remainder of this chapter I will describe this new technique and review its historical background.

1.2 D_A and the transmission probability density function

Oke and Korycansky (1982) were the first to introduce the concept of the "flux deficit" parameter D_A which is defined by

$$D_A = \left\langle 1 - \frac{f_\nu(observed)}{f_\nu(continuum)} \right\rangle \tag{1.1}$$

where the average is taken over the entire wavelength range between Lyα and Lyβ emission lines. The early measurements of D_A (Bechtold et al. 1984, Steidel & Sargent 1987, O'Brien et al. 1988) were used to quantify the reddening effect of Lyα absorption on quasar spectra. The correlation of D_A and redshift found by these investigators strongly supported the view that the absorption was caused by *intervening* material rather than by some intrinsic property of the quasars. Soon it was realised that the concept of D_A could be extended to a new approach in analysing the statistical properties of the Lyα forest: the idea is to view a quasar spectrum as a stochastic process. The intensity at each point (pixel) of a (normalised) spectrum is a random variable that is drawn from some transmission probability density function (tpdf). This pdf can be visualised as the histogram of pixel intensities of a spectrum and varies with redshift, i.e. its properties such as the n-th moments will be functions of wavelength.

From an abstract point of view, this approach must be considered superior to the traditional line counting technique because it does not involve the elaborate process of line fitting which introduces many uncertainties and is very sensitive to spectral resolution and the signal to noise ratio. In addition, line counting is severely hampered by line blending effects due to the intrinsic widths of absorption lines and spectral resolution as mentioned earlier. Nevertheless, line counting statistics have already provided us with valuable information and are indispensable in many areas of research. On the other hand, working with the tpdf involves *only* the data itself and is fairly insensitive to spectral resolution and noise. Using this approach one can obtain many statistical properties of the Lyα forest without actually resolving any single cloud. The biggest problem associated with this method is the uncertainty that is introduced by our ignorance of the exact location of the continuum. The contamination of the Lyα forest with unidentified metal lines is a problem inherent to both line counting and tpdf analysis.

Several investigators have already recognised the merits of dealing with the tpdf rather than with line lists and numerous aspects of the Lyα forest have been thus investigated:

Jenkins and Ostriker (1991) used not only D_A but also the shape of the tpdf to constrain the Gunn-Peterson effect, the continuous absorption caused by a smooth distribution of neutral hydrogen in the intergalactic medium.

Webb et al. (1992) employed a similar technique towards the same end, but explicitly examined the tpdf in those spectral regions where no significant discrete lines were detected.

Zuo and Zuo and Phinney (1993, 1993) developed analytical calculations on the tpdf and clarified the relation between D_A and the tpdf.

Zuo and Lu (1993) used the evolution of the mean of the tpdf to measure γ, the power law index of the number density evolution of Lyα clouds as a function of redshift.

Similarly, Press et al. (1993) also measured the mean absorption in terms of D_A and were the first (and to my knowledge remain so far the *only* ones) to remark on fluctuations of this around the mean. They found that these fluctuations were slightly larger than expected from an uncorrelated distribution of clouds. In a follow-up paper (Press & Rybicki 1993) they used the variance of the tpdf to put upper limits on the cloud-cloud correlation function ξ.

Zuo and Bond (1994) investigated this possibility in some detail and also attempted to measure the pixel-pixel correlation function.

Rauch et al. (1997) used the observed *cumulative* tpdf in comparison to ones produced by hydrodynamical simulations of hierarchical clustering models to

obtain a constraint on Ω_b, the baryonic density.
Similarly, Cen (1997) speculated on the possibility of using the high end of the tpdf to constrain cosmological parameters.

1.3 A new analysis

As pointed out, so far virtually no attention has been paid to the possibility of detecting large structures in the Lyα forest using the tpdf, although it should be clear that any non-random irregularities in the Lyα forest will impress themselves onto the properties of the transmission pdf. Thus I propose a *new* method to search for non-randomness in the Lyα forest:
As will be shown in section 2.3, a measurement of $1 - D_A$ is in effect a measurement of the mean (1st moment) of the tpdf at the central wavelength of the spectral range that is used to compute $1 - D_A$. Once this has been realised it seems helpful *not* to measure $1 - D_A$ by averaging over the entire data as is usually done, but to measure it as a function of wavelength by using only small, successive portions of the data. By varying the size of these portions from just one pixel to the extent of the entire accessible wavelength range one moves smoothly from the spectrum itself to a point where the entire spectrum is compressed into a single number, namely $1 - D_A$. Mathematically, this procedure corresponds to convolving the spectrum with a top-hat function of varying size. So, essentially the technique proposed here consists of sliding a window of given size across the spectrum and repeating this process for all possible window sizes. The result is a "transmission surface" — $1 - D_A$ as a function of wavelength and window size. Of course, this procedure benefits from all the advantages of working with the tpdf, but also suffers the same drawback of having to fit the continuum as accurately as possible. Although $1 - D_A$ itself is fairly insensitive to spectral resolution and signal to noise ratio, it *does* help to employ high quality spectra when fitting the continuum. One more advantage of this new technique over line counting should be pointed out: It is exceedingly simple to apply to real data whereas even semi-automated line fitting procedures are a tedious affair.

As we shall see in chapter 2 the expectation value and the variance of $1 - D_A$

can be calculated semi-analytically as functions of wavelength and window size and the effects of finite spectral resolution and limited signal to noise ratio can be reliably accounted for. Thus we can compare measured values of $1 - D_A$ with their expected values and assess the statistical significance of any fluctuations.

The procedure described above extends naturally to the case of multiple lines of sight by simply computing $1 - D_A$ using *all* the available data for a given wavelength and window size. Of course this only makes sense if one uses lines of sight that are spaced fairly closely, hoping that large structures of absorbers intersect all lines of sight.

Chapter 2

Theory

In this chapter I will review the theoretical background and derive the equations that will be needed in later chapters.

2.1 Relativistic Cosmology

In the framework of general relativity, the cosmological principle of large-scale homogeneity and isotropy leads to a Robertson-Walker metric (Misner et al. 1973):

$$ds^2 = -c^2 dt^2 + a^2(t)[d\chi^2 + \Sigma^2(\chi)(d\theta^2 + \sin^2\theta\, d\phi^2)], \tag{2.1}$$

where t denotes a cosmic time coordinate, χ, θ and ϕ are the three spatial, comoving coordinates, $a(t)$ is the scale factor of the Universe, and

$$\begin{array}{rcllll}\Sigma(\chi) & = & \sin\chi & \text{if } k = +1 & \text{(positive curvature)} \\ \Sigma(\chi) & = & \chi & \text{if } k = 0 & \text{(zero curvature)} \\ \Sigma(\chi) & = & \sinh\chi & \text{if } k = -1 & \text{(negative curvature)}\end{array}$$

The Einstein field equation[1]

$$\mathbf{G} = 8\pi G\mathbf{T}, \tag{2.2}$$

[1]For simplicity I will assume $\Lambda = 0$ throughout this work.

where $\mathbf{G}$ is the Einstein tensor, $\mathbf{T}$ denotes the stress-energy tensor, and G is Newton's gravitational constant, yields

$$G_{tt} = 3\left(\frac{\dot{a}}{a}\right)^2 + 3\frac{kc^2}{a^2} = 8\pi G\rho \tag{2.3}$$

and

$$G_{\chi\chi} = G_{\theta\theta} = G_{\phi\phi} = -2\frac{\ddot{a}}{a} - \left(\frac{\dot{a}}{a}\right)^2 - \frac{kc^2}{a^2} = 8\pi G\frac{p}{c^2}, \tag{2.4}$$

where $p = p(t)$ and $\rho = \rho(t)$ denote the pressure and density of the Universe and c is the velocity of light. In general, ρ (p) is the sum of the densities (pressures) of matter and radiation. At the present epoch though we can neglect ρ_r and thus we have (conservation of matter)

$$\rho a^3 = \rho_0 a_0^3 = const. \tag{2.5}$$

Throughout this section the subscript 0 denotes today's value of a quantity.

Together with an equation of state, $p = p(\rho)$, equations (2.3) and (2.4) give a complete dynamical description of space-time geometry.

2.1.1 Distances

When dealing with large scale structure one frequently has to calculate the distance between two objects at given redshifts. The redshift is a consequence of the expansion of the Universe and an object is said to be at redshift z if the emitted (rest-frame) and observed wavelengths obey

$$z = \frac{\lambda_{\rm obs} - \lambda_{\rm rest}}{\lambda_{\rm rest}}. \tag{2.6}$$

It can easily be shown (Misner et al. 1973) that

$$a = \frac{a_0}{1+z}. \tag{2.7}$$

The *comoving* distance is the co-ordinate distance as defined by (2.1). The comoving distance between two objects that take part in the universal expansion (e.g. two galaxies that are far apart) does not change over time. The *proper* distance is the physical distance as measured with a rigid ruler. The proper distance between two objects that are somehow held together (e.g. two gravitationally bound galaxies or the endpoints of a rod) does not change over time. In contrast, the comoving distance of two such objects *does* change since their comoving co-ordinates change. If one works in units where $a_0 = 1$ then the proper distance of two points in space *today* is equal to the comoving distance of those points.

Given the angle α that a rod at redshift z subtends, what is its length l? More precisely, what is the proper distance, *at the time of emission* between the two points of space that were located at the ends of the rod at the time of emission. To answer this question, recall that in the case $k = 1$ the spatial part of (2.1) is the metric of a 3-sphere. For illustrative purposes we can revert to the two-dimensional case ($k = 1$): space is the surface of a conventional sphere and for a point $P(\chi, \phi)$, χ gives the angle between P and one of the poles. Imagine a rod at $\chi(z)$ perpendicular to the line of sight and the observer at the pole. For each end point of the rod there exists one and only one null geodesic that connects it with the pole (observer). The angle between those two geodesics at the pole is of course α. At the time of emission the distance of the rod to the axis of the sphere is simply $a \sin\chi$ and at the axis at that time it also subtends the angle α. Thus l is simply given by

$$l = \alpha\, a\, \Sigma(\chi) = \alpha\, \frac{a_0 \Sigma(\chi)}{1+z}. \tag{2.8}$$

This formula is also correct for three spatial dimensions and for all k (Misner et al. 1973).

2.1.2 The comoving volume element

In chapter 3 I will need the formula for the comoving volume element, dV_0, as a function of redshift. We have (Misner et al. 1973)

$$dV_0 = a_0^3\, \Sigma^2(\chi)\, d\chi\, d\Omega, \tag{2.9}$$

where $d\Omega = \sin\theta \, d\theta \, d\phi$. For a photon which travels along a null geodesic ($ds^2 = 0$) we have from (2.1) ($d\theta = d\phi = 0$):

$$\chi = \int_{t_e}^{t_o} \frac{c}{a} \, dt = \int_{a(t_e)}^{a(t_o)} \frac{c}{a\dot{a}} \, da, \tag{2.10}$$

where t_e and t_o are the times of emission and observation of the photon. Using the definitions of the Hubble constant $H \equiv \dot{a}/a$ and the density parameter $\Omega \equiv 8\pi G\rho/(3H^2)$ we find from (2.3):

$$kc^2 = a^2 \Omega H^2 - \dot{a}^2 = a^2 H^2 (\Omega - 1) = a_0^2 H_0^2 (\Omega_0 - 1). \tag{2.11}$$

Using (2.5) we find

$$\dot{a}^2 = \Omega_0 H_0^2 \, \frac{a_0^3}{a} - a_0^2 H_0^2 (\Omega_0 - 1). \tag{2.12}$$

Substituting this into equation (2.10) we find for the case $k = 1$:

$$\begin{aligned} d\chi &= \frac{c}{a_0 H_0} \, \frac{1}{(1+z)\sqrt{1+\Omega_0 z}} \, dz & (2.13) \\ \chi &= \frac{c}{a_0 H_0} \, \frac{2}{\sqrt{\Omega_0 - 1}} \int_{\sqrt{\frac{1}{1+z}}}^{1} \frac{1}{(-x^2 + \frac{\Omega_0}{\Omega_0 - 1})^{1/2}} \, dx & \\ &= 2 \left(\arcsin \sqrt{\frac{\Omega_0 - 1}{\Omega_0}} - \arcsin \sqrt{\frac{\Omega_0 - 1}{\Omega_0 (1+z)}} \right). & (2.14) \end{aligned}$$

Introducing the deceleration parameter $q \equiv a\ddot{a}/a^2 = \Omega/2$, we have

$$\begin{aligned} \Sigma(\chi) &= \sin\chi \\ &= \frac{c}{a_0 H_0 q_0^2} \, (1+z)^{-1} \left[q_0 z + (q_0 - 1) \left(\sqrt{1 + 2q_0 z} - 1 \right) \right]. \end{aligned} \tag{2.15}$$

In general,

$$\begin{aligned} \frac{dV_0}{dz} &= \frac{\Omega \, c \, a_0^2 \Sigma^2(\chi)}{H_0 \, (1+z) \, (1 + 2q_0 z)^{1/2}} \\ &= \frac{\Omega \, c^3}{H_0^3 q_0^4} \, \frac{\left[q_0 z + (q_0 - 1) \, (\sqrt{1 + 2q_0 z} - 1) \right]^2}{(1+z)^3 \, (1 + 2q_0 z)^{1/2}}. \end{aligned} \tag{2.16}$$

Figure 1 shows dV_0/dz as a function of z and q_0. For $q_0 = 1/2$, dV_0/dz peaks at $z \approx 1.5$. For larger z, dV_0/dz increases steeply towards smaller q_0 because in a low mass Universe the expansion proceeds quicker than in a high mass Universe.

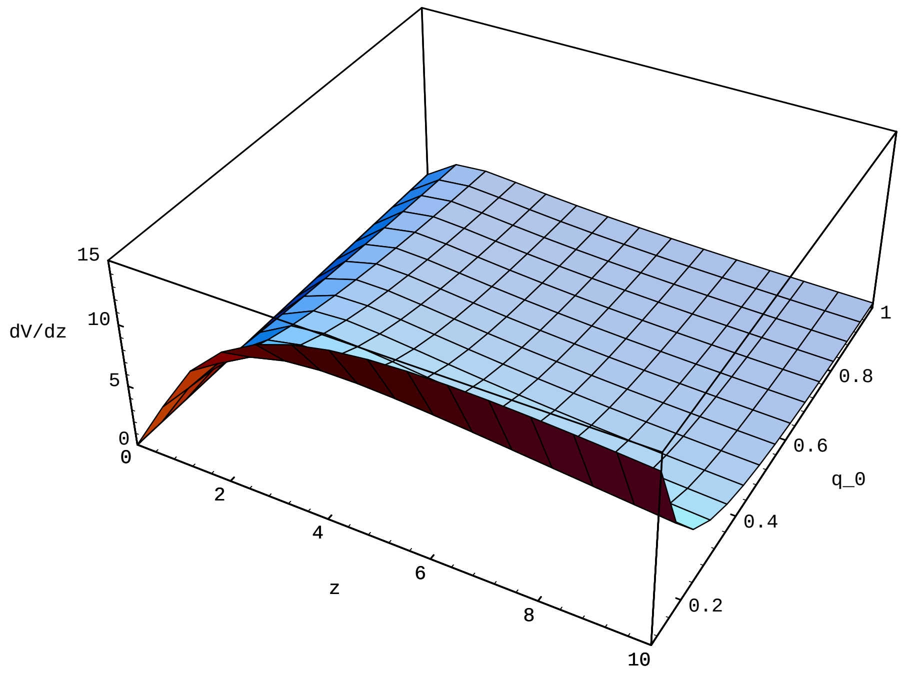

Fig. 1.— $\frac{dV_0}{dz}$ in units of $10^9\ h_{100}^{-3}$ Mpc^3 for $\Omega = 1$ sterad.

2.2 The transmission pdf

In this section I will develop the theoretical background of the new analysis technique presented here.

From now on we shall consider a normalised spectrum to be a *stochastic process* (Jenkins & Watts 1968). Every point (pixel) of the spectrum is a random variable, called $e^{-\tau(\lambda)}$, drawn from a probability density function (pdf) $f_{e^{-\tau(\lambda)}}$. In principle, we have a different pdf for every λ, meaning that the parameters of the pdf (such as the n-th moment) are functions of λ also.

In sections 2.2.1 and 2.2.2 I follow the work of Zuo et al. (Zuo & Phinney 1993, Zuo 1993) in calculating the mean and variance of $e^{-\tau}$. Then I will investigate the effects of finite spectral resolution and instrument noise on those quantities. Finally, I derive the mean and variance of the variable $1 - D_A$.

2.2.1 The mean

Given the distribution of clouds $\frac{d\#}{dz\,dN\,db} = \eta(z, N, b)$, what is the mean transmission at a given wavelength? We can define an effective optical depth $\tau_{\rm eff}$ by

$$e^{-\tau_{\rm eff}(\lambda)} := \left\langle e^{-\tau(\lambda)} \right\rangle \tag{2.17}$$

In the following I will neglect any absorption caused by smoothly distributed gas (Gunn-Peterson effect). If it exists at all it is limited to having a very small effect on $\tau_{\rm eff}$ of 0.04 at the most (Webb et al. 1992). If the number of clouds per sightline is Poisson distributed with a mean of $m = \int_0^\infty \int_0^\infty \int_0^{z_{\rm em}} \eta(z, N, b)\, dz\, dN\, db$ then we have

$$e^{-\tau_{\rm eff}} = \sum_{k=0}^{\infty} p(k; m) \langle e^{-\tau_{\rm c}} \rangle^k, \tag{2.18}$$

where $p(k; m) = e^{-m}\, m^k / \, k!$ is the probability of the sightline intersecting k clouds and

$$\left\langle e^{-\tau_{\rm c}(\lambda)} \right\rangle = \int_0^\infty \int_0^\infty \int_0^{z_{\rm em}} \frac{\eta(z, N, b)}{m} e^{-\tau_{\rm c}(\lambda_z; N, b)}\, dz\, dN\, db. \tag{2.19}$$

$\tau_c(\lambda_z;\, N, b)$ is the absorption profile produced by a single cloud at z, N, b where $\lambda_z = \lambda/(1+z)$. After some algebra we find

$$\begin{aligned}
\tau_{\rm eff} = m(1 - \langle e^{-\tau_c}\rangle) &= \int \eta(1 - e^{-\tau_c(\lambda_z)})\, dz\, dN\, db \\
&= \lambda \int_0^\infty \int_0^\infty \int_{\frac{\lambda}{1+z_{\rm em}}}^{\lambda} \frac{\eta}{\lambda_z^2}(1 - e^{-\tau_c(\lambda_z)})\, d\lambda_z\, dN\, db
\end{aligned} \tag{2.20}$$

At this point it is necessary to consider the optical depth τ_c in more detail. In general, τ_c is given by (Lang 1980):

$$\tau_c = N\,\alpha\, H(a, \nu), \tag{2.21}$$

where α is the absorption cross-section. The Voigt-function H is defined as

$$H(a, \nu) = \frac{a}{\pi} \int_{-\infty}^{\infty} \frac{e^{-y^2}}{a^2 + (\nu - y)^2}\, dy, \tag{2.22}$$

where

$$\begin{aligned}
a &= \frac{\Gamma\, \lambda_0}{4\pi b} \\
\nu &= \frac{c}{b}\left(\frac{\lambda_0}{\lambda} - 1\right),
\end{aligned}$$

Γ being the damping constant and λ_0 the central rest-wavelength of the absorption line. For Lyα absorption we have $\lambda_0 = \lambda_\alpha = 1215.67$ Å. We see that $\tau_c(\lambda_z)$ peaks sharply at $\lambda_z = \lambda_\alpha$ so that

$$\tau_{\rm eff} \simeq \frac{1 + z_{\rm abs}}{\lambda_\alpha} \iint \eta(z_{abs}, N, b) \int_{\frac{\lambda}{1+z_{\rm em}}}^{\lambda} (1 - e^{-\tau_c(\lambda_z)})\, d\lambda_z\, dN\, db, \tag{2.23}$$

where $z_{\rm abs} = \lambda/\lambda_\alpha - 1$. At this point it is helpful to introduce the rest equivalent width W

$$W(N, b) = \int_0^\infty (1 - e^{-\tau_c(\lambda; N, b)})\, d\lambda. \tag{2.24}$$

Since we are observing at $z > 2$ we can extend the upper limit of the integration over λ_z in (2.23) to ∞ and if λ is well below $\lambda_{\rm em} = \lambda_\alpha(1 + z_{\rm em})$ we can extend the lower limit to 0 because if λ_z and λ_α are sufficiently far apart, $1 - e^{-\tau_c}$ is zero. Thus we have

$$\tau_{\rm eff} \simeq \frac{1 + z_{\rm abs}}{\lambda_\alpha} \int \eta(z_{\rm abs}, N, b)\, W(N, b)\, dN\, db. \tag{2.25}$$

Note that for λ close to $\lambda_{\rm em}$, $\tau_{\rm eff}$ is smaller than predicted by the above equation because far from $\lambda_{\rm em}$ the absorption at λ is caused not only by lines right at λ but also by the wings of the lines just shortward and longward of λ. Close to $\lambda_{\rm em}$ on the other hand, the longward lines are missing because clouds that are physically *behind* the QSO cannot cause any absorption. In reality, this "edge effect" will be superimposed on the well-known proximity effect (Weymann et al. 1981, Cooke et al. 1997) which describes the decrease in absorption line density close to the redshift of the background quasar due to a higher ionisation level caused by the quasar's ultraviolet radiation. Similarly, there will be a reverse edge effect for λ close to $\lambda_\beta(1+z_{\rm em})$ because of the additional absorption by Lyβ lines.

As we shall see in chapter 3, η is found observationally to be of the form $\eta(z,N,b) = (1+z)^\gamma F(N,b)$. We therefore arrive at

$$\tau_{\rm eff} = B(1+z_{\rm abs})^{\gamma+1} = B\left(\frac{\lambda}{\lambda_\alpha}\right)^{\gamma+1}, \tag{2.26}$$

where

$$B = \frac{1}{\lambda_\alpha}\int_0^\infty\int_0^\infty F(N,b)\,W(N,b)\,dN\,db. \tag{2.27}$$

Thus we have

$$\left\langle e^{-\tau}\right\rangle = e^{-B\left(\frac{\lambda}{\lambda_\alpha}\right)^{\gamma+1}} = e^{-B(1+z)^{\gamma+1}}. \tag{2.28}$$

Effectively, γ determines the functional form of $e^{-\tau_{\rm eff}}$ whereas B contains the normalisation.

2.2.2 The auto-covariance

The auto-covariance function of the transmission is given by

$$\begin{aligned} \gamma_{e^{-\tau}}(\lambda,\lambda') &= \left\langle\left(e^{-\tau(\lambda)} - \left\langle e^{-\tau(\lambda)}\right\rangle\right)\left(e^{-\tau(\lambda')} - \left\langle e^{-\tau(\lambda')}\right\rangle\right)\right\rangle \\ &= \left\langle e^{-\tau(\lambda)}e^{-\tau(\lambda')}\right\rangle - e^{-\tau_{\rm eff}(\lambda)}e^{-\tau_{\rm eff}(\lambda')} \\ &=: e^{-\Pi(\lambda,\lambda')} - e^{-\tau_{\rm eff}(\lambda)}e^{-\tau_{\rm eff}(\lambda')}. \end{aligned} \tag{2.29}$$

Following the same calculations as in section 2.2.1, we find

$$\Pi(\lambda,\lambda') = \int \eta(z,N,b)\,(1-e^{-\tau_c(\lambda)}e^{-\tau_c(\lambda')})\,dz\,dN\,db. \tag{2.30}$$

Let us consider the variance of the transmission given by

$$\sigma^2_{e^{-\tau}} = \gamma_{e^{-\tau}}(\lambda, \lambda). \tag{2.31}$$

From (2.21) we see that

$$2\tau_c(N) = \tau_c(2N) \tag{2.32}$$

and thus we get similarly to equation (2.26)

$$\Pi(\lambda, \lambda) = \tilde{B}(1+z)^{\gamma+1}, \tag{2.33}$$

where

$$\tilde{B} = \frac{1}{\lambda_\alpha} \int_0^\infty \int_0^\infty F(N, b)\, W(2N, b)\, dN\, db. \tag{2.34}$$

If we assume (see chapter 3) that $F(N, b) = N^{-\beta} f(b)$ we have

$$\tilde{B} = \frac{2^{\beta-1}}{\lambda_\alpha} \int_0^\infty \int_0^\infty F(N, b)\, W(N, b)\, dN\, db = 2^{\beta-1} B. \tag{2.35}$$

Finally we arrive at

$$\sigma^2_{e^{-\tau}} = e^{-2^{\beta-1}B(1+z)^{\gamma+1}} - e^{-2B(1+z)^{\gamma+1}}, \tag{2.36}$$

implying $\beta < 2$. Of course if the power law in N were true for *all* N then the mean number of absorption lines per line of sight would diverge and so would τ_{eff} since for small N, W is proportional to the first power of N, but $\beta \approx 1.5$. In reality the power law must therefore break off at some N_l and $\tilde{B}$ will be smaller than $2^{\beta-1}B$.

2.2.3 Instrumental effects

So far I have not considered any instrumental effects. There are two such effects: finite spectral resolution and various sources of noise.

Finite resolution

A new stochastic variable X is produced by convolving $e^{-\tau}$ with a line spread function (LSF) G:

$$X(\lambda) = \int_{-\infty}^{\infty} e^{-\tau(\lambda')} G(\lambda - \lambda')\, d\lambda' \tag{2.37}$$

For the mean of X we get

$$\langle X \rangle = \int_{-\infty}^{\infty} \langle e^{-\tau(\lambda')} \rangle G(\lambda - \lambda')\, d\lambda'. \tag{2.38}$$

Although it has been stressed that the mean and the variance of $e^{-\tau}$ are functions of λ I will now approximate $e^{-\tau}$ as a *stationary* stochastic process because both the mean and the variance are smooth, slowly varying functions of λ. Lu and Zuo (1994) have shown this approximation to be valid. Thus we have

$$\langle X \rangle(\lambda) \simeq \langle e^{-\tau(\lambda)} \rangle \tag{2.39}$$

since the LSF is normalised to unity. As is intuitively clear, the convolution does not change the mean transmission.

The auto-covariance function of X is given by

$$\begin{aligned} \gamma_X(\lambda_1, \lambda_2) &= \langle (X(\lambda_1) - \langle X \rangle(\lambda_1))\ (X(\lambda_2) - \langle X \rangle(\lambda_2)) \rangle \\ &= \iint\limits_{-\infty}^{+\infty} G(\lambda_1 - \lambda_1')\, G(\lambda_2 - \lambda_2')\, \gamma_{e^{-\tau}}(\lambda_1', \lambda_2')\, d\lambda_1'\, d\lambda_2'. \end{aligned} \tag{2.40}$$

Since we consider $e^{-\tau}$ to be a *stationary* process, $\gamma_{e^{-\tau}}$ depends only on $u' = \lambda_2' - \lambda_1'$ and γ_X depends only on $u = \lambda_2 - \lambda_1$ (Jenkins & Watts 1968). Usually, the LSF can be well approximated as a Gaussian. After some algebra we get

$$\gamma_X(u) = \frac{1}{\sqrt{2\pi}\sigma'_{\mathrm{LSF}}} \int_{-\infty}^{\infty} \gamma_{e^{-\tau}}(u')\, \exp\left(-\frac{(u-u')^2}{2\sigma'^2_{\mathrm{LSF}}} \right) du', \tag{2.41}$$

where $\sigma'_{\mathrm{LSF}} = \sqrt{2}\, \sigma_{\mathrm{LSF}}$.

Noise

The noise in optical spectra is mainly due to photon counting statistics, detector read-out noise, dark current, sky subtraction, and cosmic rays. As the Poisson statistics of the clouds are expected to dominate the variance I shall not attempt to model the noise characteristics in great detail. Rather I shall approximate the cumulative effect of all the noise components mentioned above to be Gaussian. Therefore, I define the stochastic variable Y by

$$Y(\lambda) = X(\lambda) + n(X(\lambda)), \tag{2.42}$$

where n is a random variable drawn from a Gaussian with mean zero and variance $\sigma_n^2(X) = X\,(c_1 - c_2) + c_2$. The constants c_1 and c_2 characterise the photon counting statistics and the sky subtraction plus detector noise ($c_1 > c_2$). For the mean of Y we have

$$\langle Y \rangle \;=\; \langle X \rangle + \langle n \rangle \;=\; \langle X \rangle \;=\; \langle e^{-\tau} \rangle \tag{2.43}$$

and the covariance is given by

$$\gamma_Y(\lambda_1, \lambda_2) = \gamma_X(\lambda_1, \lambda_2) + \gamma_{Xn}(\lambda_1, \lambda_2) + \gamma_{Xn}(\lambda_2, \lambda_1) + \gamma_n(\lambda_1, \lambda_2). \tag{2.44}$$

γ_{Xn} denotes the *cross*-covariance function of X and n. Although X and n are not *independent* they are, by definition of the term "noise", *uncorrelated*, so that $\gamma_{Xn} = 0$. It is straightforward to show that $\gamma_n(u)$ is discontinuous at $u = 0$:

$$\gamma_n(u) = \begin{cases} 0 & u > 0 \\ \int f_X(x)\,\sigma_n^2(x)\,dx & u = 0 \end{cases} \tag{2.45}$$

where $f_X(x)$ denotes the pdf of X. A good approximation for the integral is $\sigma_n^2(\langle X \rangle)$. More conservatively one can use the upper limit c_1. Thus

$$\begin{aligned} \sigma_Y^2 &= \sigma_X^2 + \sigma_n^2(\langle X \rangle) \\ \gamma_Y(u) &= \gamma_X(u) \qquad\qquad u > 0. \end{aligned} \tag{2.46}$$

2.3 $1 - D_A$

Now we are in a position to calculate the expectation value (mean) and the variance of the variable that will actually be measured, $1 - D_A$:

$$(1 - D_A)_{\Delta\lambda}(\lambda) = \int_{-\infty}^{\infty} Y(\lambda')\,\vartheta_{\Delta\lambda}(\lambda - \lambda')\,d\lambda' = \frac{\int_{\lambda-\Delta\lambda}^{\lambda+\Delta\lambda} Y(\lambda')\,d\lambda'}{2\Delta\lambda} \tag{2.47}$$

where

$$\vartheta_{\Delta\lambda}(\lambda) = \frac{\Theta(\lambda + \Delta\lambda)\,\Theta(\lambda - \Delta\lambda)}{2\Delta\lambda},$$

and $\Theta(\lambda)$ denotes the Heaviside step function. Therefore

$$\langle 1 - D_A \rangle(\lambda) \;=\; \frac{\int_{\lambda-\Delta\lambda}^{\lambda+\Delta\lambda} \langle Y \rangle(\lambda')\,d\lambda'}{2\Delta\lambda} \simeq e^{-\tau_{\mathrm{eff}}(\lambda)} = e^{-B(1+z)^{\gamma+1}}. \tag{2.48}$$

Press et al. (1993) have already observationally confirmed this result. From this equation we can see that a measurement of $1 - D_A$ is in effect a measurement of $e^{-\tau_{\rm eff}}$, the mean of the transmission pdf, as was pointed out in section 1.3. We also see from equation (2.48) that the expectation value of $1 - D_A$ is *independent* of instrumental resolution and noise. In theory, this statement will only be true within certain limits (because of the approximation in equation (2.39)) but we shall see in chapter 3 that in practice it indeed holds for the range of instrument parameters commonly encountered today.

We see from equation (2.47) that $1 - D_A$ is the convolution of Y with a top-hat function. Similarly to equation (2.40) we thus have for the variance of $(1-D_A)_{\Delta\lambda}$:

$$\sigma^2_{\Delta\lambda}(\lambda) = \frac{1}{4(\Delta\lambda)^2} \iint\limits_{\lambda-\Delta\lambda}^{\lambda+\Delta\lambda} \gamma_Y(\lambda'_1, \lambda'_2)\, d\lambda'_1\, d\lambda'_2 \tag{2.49}$$

Again approximating Y to be a stationary process we can make the transformation

$$\begin{aligned} u &= \lambda'_1 - \lambda'_2 \\ v &= \sqrt{2}\,(\lambda'_1 + \lambda'_2) \end{aligned} \tag{2.50}$$

and get

$$\sigma^2_{\Delta\lambda} = \frac{1}{4(\Delta\lambda)^2} \int_{-2\Delta\lambda}^{2\Delta\lambda} \gamma_Y(u)\, 2\Delta\lambda \left(1 - \frac{|u|}{2\Delta\lambda}\right)\, du. \tag{2.51}$$

Introducing the autocorrelation function $\rho(u) = \gamma(u)/\gamma(0)$ $(0 \le \rho \le 1)$ and using equation (2.46) we have

$$\sigma^2_{\Delta\lambda} = \frac{\sigma^2_n(e^{-\tau_{\rm eff}})}{2\Delta\lambda} + \frac{\sigma^2_X}{2\Delta\lambda} \int_{-2\Delta\lambda}^{2\Delta\lambda} \rho_X(u) \left(1 - \frac{|u|}{2\Delta\lambda}\right)\, du. \tag{2.52}$$

In practice we must consider the discrete case (the window of length $2\Delta\lambda$ contains N pixel):

$$\sigma^2_N = \frac{\sigma^2_n(e^{-\tau_{\rm eff}})}{N} + \frac{\sigma^2_X}{N} \left(1 + 2\sum_{i=1}^{N} \rho^i_X \left(1 - \frac{i}{N}\right)\right), \tag{2.53}$$

where I have used the symmetry of the integrand of (2.52). In this form one can see best how the correlation of X influences the variance of $1 - D_A$. Let us consider the second addend of (2.53). In the case $\rho^i_X = 0\ \forall\ i$ we get σ^2_X/N which is what one would expect when averaging over N uncorrelated random variables. In the case $\rho^i_X = 1\ \forall\ i$ we get σ^2_X which is also correct, since averaging over N

numbers which all have the same (random) value is the same thing as drawing only one random number.

Equation (2.47) can easily be generalised to the case of multiple lines of sight by summing over the spectra and dividing by the number of spectra, $N_{\rm spec}$. As a result $\langle 1 - D_A \rangle$ remains unchanged and $\sigma^2_{\Delta\lambda}$ is simply divided by $N_{\rm spec}$ since the null hypothesis is that lines of sight with a reasonably large separation are uncorrelated. A prerequisite for this simple procedure is the uniformity of the spectra used in terms of resolution and signal to noise ratio.

In principle, one can compute equation (2.53) numerically using equation (2.30). Such calculations were carried out by Zuo and Bond (1994). However, it seems feasible to approximate $\gamma_{e^{-\tau}}$ by a suitable analytic function since $\gamma_{e^{-\tau}}$ is convolved with a Gaussian anyway and thus loses some of its detail. Subsequently, the results may be compared with simulations in order to determine the "goodness" of the approximation. It is reasonable to expect the width of $\gamma_{e^{-\tau}}$ to be of the order of a few b_0, where b_0 is the mode of the b parameter distribution (see chapter 3). Let us assume

$$\gamma_{e^{-\tau}}(u) = \sigma^2_{e^{-\tau}} \ \exp\left(-\frac{u^2}{2(qb_0/c\lambda_{\rm c})^2}\right), \tag{2.54}$$

where $\lambda_{\rm c}$ is the central wavelength of the wavelength range under consideration and q is a number of the order of 1. We have

$$\gamma_X(u) = \frac{\sigma^2_{e^{-\tau}}}{\sqrt{2\left(\frac{\sigma_{\rm LSF}}{q\,b_0/c\,\lambda_{\rm c}}\right)^2 + 1}} \ \exp\left(-\frac{u^2}{2(2\sigma^2_{\rm LSF} + (q\,b_0/c\,\lambda_{\rm c})^2)}\right) \tag{2.55}$$

and

$$\begin{aligned}\sigma^2_{\Delta\lambda}(\lambda) \ &= \ \frac{\sigma^2_n(e^{-\tau_{\rm eff}(\lambda)})}{2\Delta\lambda} + \frac{e^{-\tilde{B}(\lambda/\lambda_\alpha)^{\gamma+1}} - e^{-2B(\lambda/\lambda_\alpha)^{\gamma+1}}}{2\Delta\lambda\sqrt{2\left(\frac{\sigma_{\rm LSF}}{q\,b_0/c\,\lambda_{\rm c}}\right)^2+1}} \\ &\times 2\int_0^{2\Delta\lambda} \exp\left(-\frac{u^2}{2(2\sigma^2_{\rm LSF} + (q\,b_0/c\,\lambda_{\rm c})^2)}\right)\left(1 - \frac{u}{2\Delta\lambda}\right)\,du. \end{aligned} \tag{2.56}$$

Modern high resolution echelle spectrographs such as HIRES on the Keck telescope achieve a resolution of $\sim$ 6 km/s FWHM. In this case we have $\sigma_{\rm LSF} \ll q\,b_0$ and the $\sigma_{\rm LSF}$ terms can be neglected.

2.4 Expected sensitivity

With all the calculations in place one can now ask what the expected signal is for a given overdensity of a given size at a given redshift. In other words, how overdense must a region be in order to be distinguishable from random fluctuations?

In order to assess the statistical significance of a signal we subtract $\langle 1 - D_A \rangle$ from the measured value of $1 - D_A$ and divide by $\sigma_{\Delta\lambda}$. The result is of course a function of wavelength (redshift) and the window size $\Delta\lambda$. For a region of absorber density n we expect

$$S(\delta n) = \frac{e^{-\delta n B(1+z)^{\gamma+1}} - e^{-B(1+z)^{\gamma+1}}}{\sigma_{\Delta\lambda}(z)}, \tag{2.57}$$

where $\delta n = n/n_0$ is the fractional overdensity. Figure 2 shows a plot of $S(\delta n)$ for different redshifts and a window size which corresponds to 2 h_{100}^{-1} Mpc proper ($q_0 = 1/2$, $h_{100} = H_0/(100\ \mathrm{km/s/Mpc})$). The values of the parameters B, $\tilde{B}$, and q that were used in this plot are determined in chapter 4. We can see that at $z = 3$ an overdensity of $\delta n = 2.5$ produces a $\sim 4\sigma$ event. This is rather encouraging since the spikes in the galaxy redshift distribution found by Broadhurst et al. (1990) show an overdensity of ~ 4. We also see that the $z = 6$ curve saturates at $\sim 5.5\sigma$. For smaller window sizes this value goes down meaning that it is not all that unlikely to have total absorption in the entire window which is of course true due to the high number of absorption lines at $z = 6$. In such a case it would be impossible to tell a true, non-random overdensity from a random fluctuation. However, in all practical cases this situation will not occur.

At this point we must recall what we mean by the statement "X is a 3σ event". Ignoring instrumental effects for the moment, $(1 - D_A)_N$ is essentially the average of N $e^{-\tau}$s. Thus the pdf of $1 - D_A$, f_{1-D_A}, is essentially an N-convolution of the pdf of $e^{-\tau}$. The central limit theorem tells us that for $N \to \infty$, f_{1-D_A} tends towards a Gaussian no matter what $f_{e^{-\tau}}$ looks like. However, the central limit theorem also tells us that this convergence is faster close to the mean than far from it. That is to say that while we expect the probability of $1 - D_A$ lying within *one* $\sigma_{\Delta\lambda}$ of $e^{-\tau_{\text{eff}}}$ to be 0.68, we do *not* expect the probability of $1 - D_A$ lying within *three* $\sigma_{\Delta\lambda}$ of $e^{-\tau_{\text{eff}}}$ to be 0.9973 as would be expected for a Gaussian

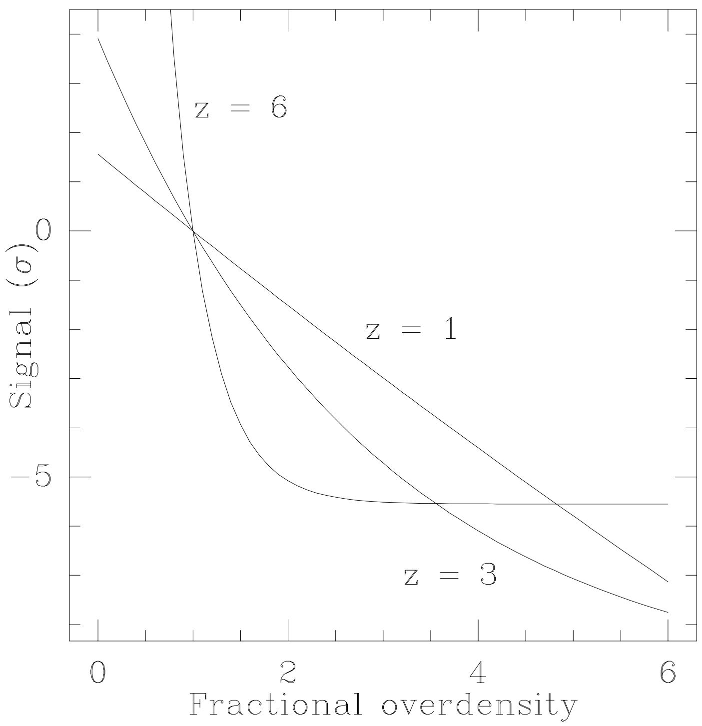

Fig. 2.— Expected signal in units of $\sigma_{\Delta\lambda}$ from a region of 2 h_{100}^{-1} Mpc proper size at various redshifts.

distribution. Rather, this probability will be somewhat lower. This is apparent from the intrinsic asymmetry of f_{1-D_A} and suggests that the 3rd moment, or skew, of f_{1-D_A} holds important information. This behaviour has also been verified experimentally using the simulations.

Chapter 3

The Simulations

The simulation of Lyα forest spectra described in this chapter are based on a semi-phenomenological model of the origin of Lyα absorption lines. This model does *not* claim to describe physical reality accurately. Rather it should be viewed as a working hypothesis built on observational results and designed to reproduce the statistical properties of the Lyα forest. The simulations were meant to

- help develop new tools to analyse not just individual, but *several*, possibly correlated, QSO spectra in order to detect the presence (or absence) of large scale structure;
- test analytical models;
- explore the effects of various large scale structure scenarios on Lyα forest spectra;
- test the reliability of the traditional technique of analysis in detecting such effects.

In addition, the simulations were required to mimic "real" spectra in the sense that noise and finite instrumental resolution were included in order to be able to study the influence of these parameters on the analysis.

Existing simulations of Lyα forest spectra can be classified into two categories:

1. Extensive smoothed particle hydrodynamical simulations (Hernquist et al. 1996, Miralda-Escudé et al. 1996, Zhang et al. 1995, Cen & Simcoe 1997), based on the current understanding of structure formation, simulate the behaviour of matter (and dark matter) in a given cosmological volume. Sightlines are then taken through this volume and the results of the analysis of the resulting spectra are compared to observations. It is the goal of such simulations to gain a better understanding of the mechanisms of structure formation.

2. In contrast, many observers have simulated the spectra themselves rather than the distribution of matter which causes the absorption (Lu et al. 1996, Ulmer 1996). These Monte Carlo simulations usually serve as the null-hypothesis with which to compare the observations. Examples are the correction for line-blending effects and the measurement of the two-point correlation function.

In structure the simulation presented here is like those in category 1 since it is one of the aims of the simulation to investigate the use of multiple, closely spaced sightlines. Before I go on to describe the details of the simulation let us consider the observed statistical properties of the Lyα forest and how they can be understood in a simple physical model.

3.1 The observed line distribution

Analogous to equation (2.8) we have for a disk of radius r_0

$$\pi r_0^2 = \left(\frac{a_0 \Sigma(\chi)}{1+z}\right)^2 \Delta\Omega$$

or

$$a_0^2 \Sigma^2(\chi) \Delta\Omega = \pi r_0^2 (1+z)^2. \tag{3.1}$$

Thus the number of clouds with radius $r \in [r, r+dr]$ and redshift $z \in [z, z+dz]$ is given by

$$d\# \quad = \quad \frac{d\#}{dV_0} dV_0$$

$$
\begin{aligned}
&= n_0\, a_0 d\chi\, a_0^2 \Sigma^2(\chi)\, d\Omega \\
&= n_0\, a_0 d\chi\, (1+z)^2\, 2\pi r\, dr \\
&= n_0 \frac{c}{H_0} 2\pi r \frac{1+z}{\sqrt{1+2q_0 z}} dz dr,
\end{aligned} \tag{3.2}
$$

where n_0 is the comoving number density of clouds. In the last step I have used equation (2.13). If we now assume that the neutral hydrogen column density N within a cloud as a function of radius is given by

$$
N(r) = N_0 \left(\frac{r}{r_0}\right)^{-a} \qquad a > 0 \tag{3.3}
$$

and

$$
\begin{aligned}
r &= r_0 \left(\frac{N}{N_0}\right)^{-\frac{1}{a}} \\
dr &= \frac{1}{a} \frac{r_0}{N_0^{-1/a}} N^{-\frac{1}{a}-1}\, dN \qquad (dN > 0),
\end{aligned}
$$

then we get

$$
\frac{d\#}{dz\, dN} = \frac{2\pi n_0 c}{a H_0} \left(\frac{r_0}{N_0^{-1/a}}\right)^2 \frac{1+z}{\sqrt{1+2q_0 z}} N^{-\frac{2}{a}-1}. \tag{3.4}
$$

Many observations (Carswell et al. 1984, Kirkman & Tytler 1997, Lu et al. 1996, Hu et al. 1995) have indeed shown that $d\#/dN \propto N^{-\beta}$ for the regime 10^{13} $\mathrm{cm}^{-2} \leq N \leq 10^{16}$ cm^{-2}. If we set

$$
a = \frac{2}{\beta - 1} \tag{3.5}
$$

then assumption (3.3) is at least not inconsistent with observations[1]. In fact, Lanzetta et al. (1995) have reported an anti-correlation of column density and impact parameter of the kind described by (3.3) and their value of $a \simeq 4$ (Webb 1996) is in good agreement with $\beta \simeq 1.5$ as found recently by Lu (1996). It should be noted that Lanzetta et al.'s measurement of (3.3) was carried out at $z \simeq 1/2$ whereas the above mentioned measurements of β were carried out at $z > 2$. It should also be pointed out that some authors (Carswell et al. 1987,

[1]Note that if the relationship (3.3) were true for *all* N then equation (2.36) would imply $a > 2$ (see also section 2.2.2).

Cristiani 1995, Khare et al. 1997) claim to have found a break in the column density distribution or even more detailed structure (Petitjean et al. 1993).

In contrast to (3.4) observations have shown the line distribution as a function of redshift to be of the form $d\#/dz \propto (1+z)^\gamma$ (Carswell et al. 1984, Kirkman & Tytler 1997, Lu et al. 1996, Williger et al. 1994), suggesting evolution of either the number density n_0 or the cross-section r_0 of the absorbers. If we choose to keep n_0 constant then we can match the observations by replacing r_0 by

$$r_0(z) = r_0\left(z = \frac{1}{2}\right) \frac{(1+2q_0 z)^{\frac{1}{4}}\,(1+z)^{\frac{\gamma-1}{2}}}{(1+q_0)^{\frac{1}{4}}\,\left(\frac{3}{2}\right)^{\frac{\gamma-1}{2}}}. \tag{3.6}$$

In addition, it has been found (Carswell et al. 1984, Kirkman & Tytler 1997, Lu et al. 1996, Hu et al. 1995) that the distribution of b parameters is of the form $d\#/db \propto \exp(-\frac{(b-\mu_b)^2}{2\sigma_b^2})$ with no lines being found with $b < b_{\rm cut}$. Thus, the distribution of absorption lines can be written as

$$\begin{aligned} \frac{d\#}{dz\,dN\,db} &= \frac{\pi n_0 c}{H_0}(\beta-1)\left[\frac{r_0\left(\frac{1}{2}\right)}{(1+q_0)^{\frac{1}{4}}\left(\frac{3}{2}\right)^{\frac{\gamma-1}{2}}}\right]^2 \frac{1}{N_0^{1-\beta}}(1+z)^\gamma N^{-\beta} \\ &\qquad \times \frac{\exp\left(-\frac{(b-\mu_b)^2}{2\sigma_b^2}\right)}{\int\limits_{b_{\rm cut}}^{\infty}\exp\left(-\frac{(b-\mu_b)^2}{2\sigma_b^2}\right)db}\,\Theta(b-b_{\rm cut}), \end{aligned} \tag{3.7}$$

where $\Theta(x)$ denotes the Heaviside step function.

3.1.1 Normalisation

We can derive an estimate of n_0 (under the above assumptions) by integrating equation (3.7) over z, N, and b between $[z_{\rm min}, z_{\rm max}]$, $[N_{\rm l}, N_{\rm u}]$, and $[b_{\rm cut}, \infty]$ and setting it equal to the observed number of absorption lines between those limits. From Lu's observation of Q0000-26 (1996) I have found 187 absorption lines with $3.4255 \leq z \leq 3.9767$, $\log N > 13.5$ ($N_{\rm u} = \infty$), $b > 18.0$ km/s. Using $q_0 = 1/2$, $\gamma = 2.5$, and $r_0(1/2)$ (radius at which $\log N = 13.5$ was measured) $= 422\ h_{100}^{-1}$ kpc, I arrive at

$$n_0 = 8.77 \times 10^{-3}\ h_{100}^3\ {\rm Mpc}^{-3}. \tag{3.8}$$

This value is likely to be too low because of the effect of line blending. Although Lu deemed his list of absorption lines to be complete for $\log N > 13.5$ it is likely that many lines are covered by others. This problem cannot be resolved by employing higher resolution because of the intrinsic width of the absorption lines. Inserting this value into equation (3.7), we find

$$\frac{d\#}{dz\,dN\,db} = 1.4 \times 10^6\,(1+z)^\gamma\,N^{-\beta}\,e^{-\frac{(b-\mu_b)^2}{2\sigma_b^2}}\,\Theta(b-b_{\rm cut}), \tag{3.9}$$

where I have used $\beta = 1.5$, $\mu_b = 23$ km/s, $\sigma_b = 8$ km/s, and $b_{\rm cut} = 18$ km/s.

3.2 Simulating a population of absorbing galaxies

The simulation follows in principle a model first developed by Neyman and Scott (1952) and later taken up by Sheth and Saslaw (1994). This model gives a straightforward algorithm of how to distribute $N_{\rm tot}$ absorbers in a volume V:
$N_{\rm tot}$ cluster centres are put down randomly in V such that the comoving number density of cluster centres is constant.
Then N $(0 \leq N \leq N_{\rm tot})$ absorbers are associated with each cluster centre and distributed around their cluster centres according to some radial density profile (thus assuming that clusters are spherical).
The absorbers are given a random velocity with respect to the cluster centre.
The neutral hydrogen gas within the absorbers is assumed to be distributed such that the column density as a function of radius from the absorber's centre is given by a power law ($\Rightarrow$ absorbers are also spherical).
Finally, spectra of a group of background quasars are computed using Voigt profiles (see (2.21) and the following equations).

3.2.1 The distribution of cluster centres

The volume of this simulation is cone-shaped, extending from some $z_{\rm min}$ to the redshift of the highest redshift background quasar and having a diameter of two degrees. The co-ordinates used in this simulation are redshift, right ascension (RA), and declination (DEC). The co-ordinates for a particular cluster centre are drawn from the following pdfs:

$$\begin{aligned} f(RA) &= \frac{dV_0}{dRA} &\propto& \; const \\ f(DEC) &= \frac{dV_0}{dDEC} &\propto& \; \cos DEC \\ f(z) &= \frac{dV_0}{dz} &\propto& \; \frac{\left[q_0 z+(q_0-1)(\sqrt{1+2q_0 z}-1)\right]^2}{(1+z)^3(1+2q_0 z)^{1/2}} \end{aligned} \tag{3.10}$$

where I have made use of equations (2.9) (substituting RA for ϕ and DEC for θ) and (2.16). This ensures that the comoving number density of cluster centres is constant as a function of redshift. The total number of cluster centres that are put down is simply determined from the simulation volume (which can be calculated by integrating equation (2.16)) and the number density n_0 (3.8).

3.2.2 The distribution of absorbers within clusters

Each cluster centre receives N absorbers, where N is determined by the chosen clustering model as described in section 3.3. In this context the term "cluster" is used rather loosely. Since for a particular cluster $0 \leq N \leq N_{\rm tot}$, "cluster" can mean anything from "void" ($N = 0$) and "field absorber" ($N = 1$) to "group" ($N \approx 10$) or "cluster" (in the usual sense) ($N \gg 10$). In the case $N = 1$ the absorber is placed at the position of the cluster centre. For $N > 1$, the absorbers are distributed randomly and spherically symmetrically around a cluster centre where the distance is drawn from a choice of two pdfs:

$$f(r) \propto \frac{1}{r^2}$$

(isothermal sphere) as suggested by Sheth and Saslaw (1994) or

$$f(r) \propto \frac{1}{\left(1 + \frac{r^2}{r_0^2}\right)^{3/2}}$$

which is known as the King model (King 1966). All absorbers are required to have $r \leq R = 1$ Mpc. The core size r_0 of the King model is chosen to be 250 kpc (Natarajan 1996). Absorbers are assigned a peculiar velocity which is drawn

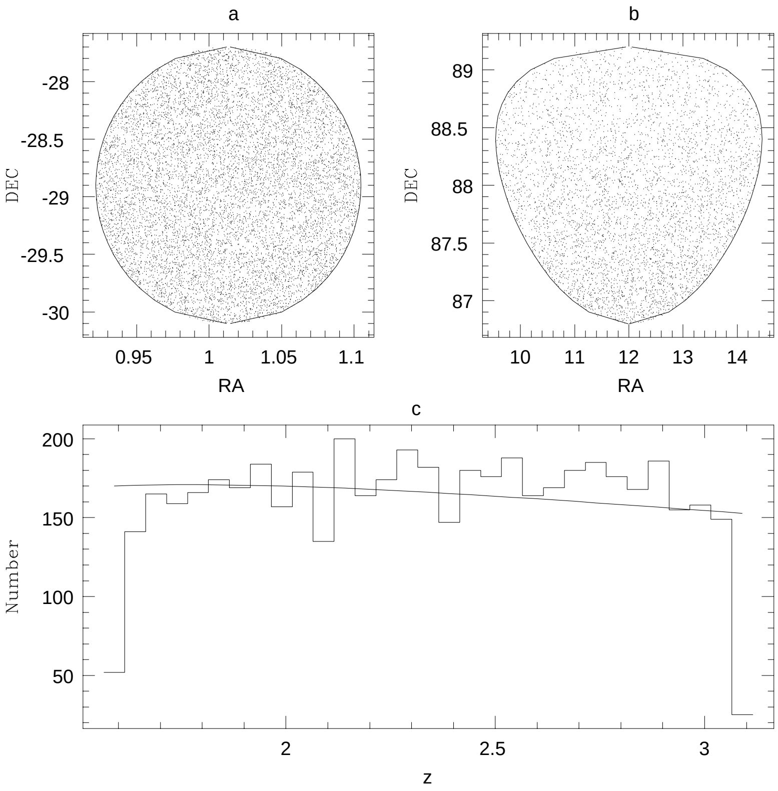

Fig. 1.— The distribution of cluster centres: Panel a shows the distribution on the sky, panel b shows the same for a high DEC case. Panel c shows the distribution of cluster centres as a function of redshift. Solid lines are theoretical curves.

from a Gaussian with $\mu = 0$ km/s and $\sigma = 500$ km/s (Fadda et al. 1996). The redshift z of the absorber is calculated from the relativistic formula

$$\frac{v_{\rm pec}}{c} = \frac{(1+z_{\rm cc})^2 - (1+z)^2}{(1+z_{\rm cc})^2 + (1+z)^2}, \tag{3.11}$$

where $z_{\rm cc}$ is the redshift of the cluster centre. This formula is derived in Appendix A.

3.2.3 Synthetic spectra

The column density N of a particular absorber is determined by calculating its distance from the sightline using equation (2.8) and then computing N from the impact parameter-N relationship (3.3) as modified by (3.6). Each absorber is also assigned a Doppler width b which corresponds to a temperature (see chapter 1) and is drawn from a Gaussian with $\mu = 23$ km/s, $\sigma = 8$ km/s and lower cutoff $b_{\rm cut} = 18$ km/s (Lu et al. 1996). With the triplet (z, N, b) known for each cloud we can proceed to include their absorption lines. This is done by the routine SPABS (Webb & Hetem 1993). Consistent with the discussion in section 2.2.2 only lines with $N > 10^{12}$ cm^{-2} are included. Below this limit the contribution to $\tau_{\rm eff}$ is expected to be negligible. Also, an upper limit of 10^{17} cm^{-2} is imposed on lines to avoid damped systems which influence the autocorrelation function $\rho_{e^{-\tau}}$. This will be discussed in more detail in section 4.1. Figure 2 shows the distribution of absorption lines that are generated by this procedure as a function of column density, redshift and, for completeness, b-parameter. As expected, we have power laws in N and z. Finally, the spectra are convolved with a Gaussian and white noise is added as described in section 2.2.3.

3.3 Clustering scenarios

In this section it should again be stressed that the simulation does *not* intend to model physical reality in all its complexity. Many simplifying assumptions have already been made and it would certainly not increase the validity of any results if one were to use a complicated clustering model which seeks to incorporate all the details of structure formation. It is planned to increase the "realness" of the simulation in the future but for the purposes of this work fairly simple models shall suffice.

I have chosen two different clustering models, the effects of which on Lyα forest spectra were explored in detail. Both models have at least *some* probability of corresponding to Nature and are straightforward to implement.

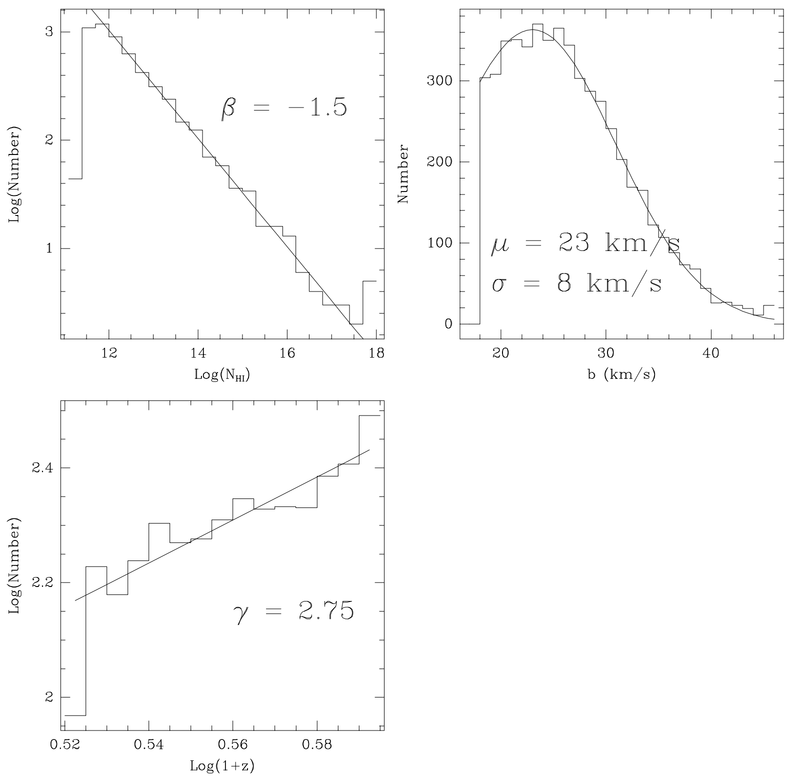

Fig. 2.— The distribution of absorption lines: Solid lines are best fits with the parameters indicated.

3.3.1 GQED

This approach implements a theory developed by Saslaw (1984) which has its foundations in the thermodynamics of gravitating systems. In essence, this theory gives the gravitational quasi-equilibrium distribution function (GQED) which is the probability of finding N galaxies in a given volume V:

$$f_V(N) = e^{-\overline{N}(1-b)-Nb}\,\frac{\overline{N}(1-b)}{N!}\left[\overline{N}(1-b)+Nb\right]^{N-1}, \tag{3.12}$$

where $\overline{N} = nV$ is the average number of galaxies expected in V with average number density n. b is defined as the ratio of gravitational potential and kinetic energies of the system (and has no connection with the Doppler parameter b of previous sections):

$$b = -\frac{W}{2K} \tag{3.13}$$

($0 \le b \le 1$). For $b = 0$, (3.12) reverts to a Poisson distribution. The generating function of $f_V(N)$, defined by

$$\mathcal{F}(s) = \sum_{N=0}^{\infty} f_V(N)\, s^N, \tag{3.14}$$

can be written as (Saslaw 1989)

$$\mathcal{F}(s) = \exp[\overline{N} + \overline{N}\mathcal{H}(s)], \tag{3.15}$$

where $\mathcal{H}(s)$ is the generating function of

$$\begin{aligned} h(0) &= b, \\ h(N > 0) &= \tfrac{N^{N-1}}{N!}\,(1-b)\, b^{N-1}\, e^{-Nb}. \end{aligned} \tag{3.16}$$

Equation (3.15) describes Poisson-distributed cluster centres where for each cluster the probability of containing N galaxies is given by $h(N)$ (Figure 3). In the case $b \to 0$ we have $h(N) \to \delta_{N,1}$ which corresponds to a Poisson-distribution of the galaxies since the cluster centres are Poisson-distributed. Note that the probability of a cluster having zero members is non-zero, which creates voids. The fundamental result which describes the evolution of b is (Saslaw 1992)

$$a = a_\star \frac{b^{1/8}}{(1-b)^{7/8}}. \tag{3.17}$$

Together with today's value of b for galaxies, $b_0 \approx 0.75$ (Sheth & Saslaw 1994), one can thus determine the strength of the clustering at a given redshift.

The connection between b and the more familiar two-point correlation function $\xi(r)$ is given by (Saslaw & Hamilton 1984)

$$b = -\frac{W}{2K} = \frac{2\pi G m^2 n}{3kT} \int_0^\infty \xi(r) r\, dr, \tag{3.18}$$

where k is the Boltzmann constant, T is the temperature of the system and m is the mass of a galaxy.

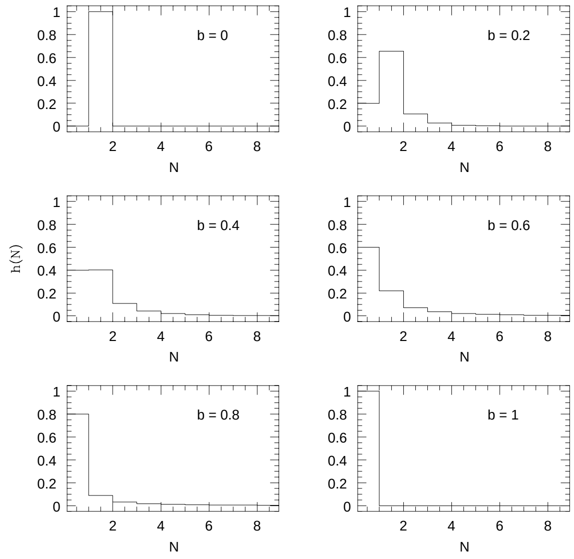

Fig. 3.— $h(N)$: Probability of a cluster having N members.

3.3.2 Walls

This model is based on the repeated findings of independent groups that galaxies form sheet- or wall-like structures which seem to exhibit some periodicity (Broadhurst et al. 1990, Ettori et al. 1997, Einasto et al. 1997, Connolly et al. 1997, Di Nella et al. 1996). From Lanzetta et al.'s findings (1995) we know that a significant percentage of Lyα lines arises in the extended haloes of galaxies. Thus it is conceivable that Lyα absorbers form similar structures. Indeed, recent observations (Crotts & Fang 1997) and results from hydrodynamic simulations (Cen & Simcoe 1997, Bond & Wadsley 1997) seem to confirm this speculation.

Walls are implemented in the simulation by simply modifying the distribution of cluster centres as a function of redshift (3.10). Instead of using dV_0/dz I use $dV_0/dz \times$ a periodic top hat function. The height of that function gives the overdensity of absorbers within the walls. As suggested by Broadhurst et al. (1990), I have chosen a period of 130 h_{100}^{-1} Mpc comoving. This corresponds to 2-3 walls between the Lyα and Lyβ emission lines of a $z \approx 2.5$ quasar. The width of walls was chosen to be a fifth of the period.

An interesting extension of the existing simulation would be the use of Voronoi Tessellations (van de Weygaert 1991) which produce foam-like structures — walls and voids.

The scenarios described above can easily be combined by simply using *both* the modified z-pdf *and* $b \neq 0$.

Chapter 4

Results from Simulations

First of all, it should be noted that the simulation actually produces spectra that are comparable with real data. To illustrate this, Figure 1 shows a simulated spectrum of Q0042-2656 at a resolution of 2 Å and a pixel size of 1 Å which can be compared directly to panel 6 of Figure 3 in chapter 5 which shows the observed spectrum of that quasar. A purely visual inspection reveals no significant differences except for a certain "waviness" of the real data around 1 which is probably due to imprecise continuum fitting. The strong absorption near 4000 Å in the simulated spectrum is due to Lyman limit absorption. The simulated data was produced using a significantly higher number density of absorbers (by almost a factor of 2) than the one given by (3.8). This is not surprising if one considers the lower panel of Figure 1. This figure shows a small part of the simulated spectrum in great detail and the individual absorption lines that were used to create this spectrum are drawn in in colour. Lu et al. (1996) considered their list of absorption lines of Q0000-26 to be complete for $\log N > 13.5$. The central relative intensity of a line with $\log N = 13.5$ and $b = 23$ km/s is ~ 0.4 and we can see from Figure 1 that even for this high value of column density any line fitting procedure will most likely return a smaller number of lines than are actually present. This figure vividly demonstrates the problems associated with line fitting. More importantly though, the simulated spectrum contains significant clustering. The absorber population is clustered according to the GQED of (3.12) with $b = 0.5$, yet a visual inspection of the upper panel of Figure

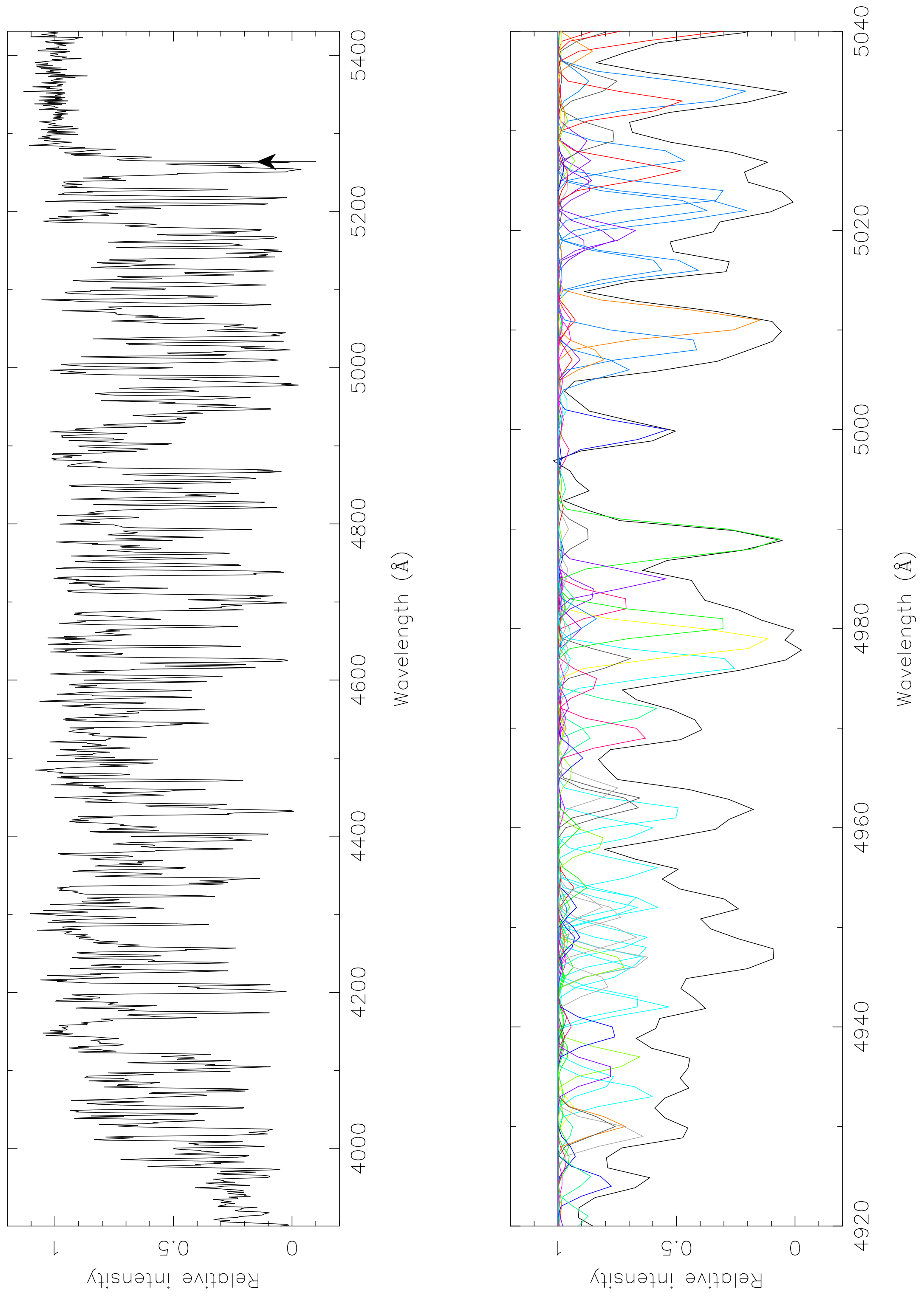

Fig. 1.— Simulated spectrum of Q0042-2656. The arrow marks the position of the Lyα emission line. The lower panel shows the constituent absorption lines (see text) for a part of the spectrum.

1 does not give a clustered impression. Absorption lines of the same colour in the lower panel of Figure 1 are caused by absorbers that are members of the same cluster. This demonstrates that clustering in the Lyα forest is not as obvious as one might think.

4.1 Tpdf

It is important to verify with the help of simulations that the theoretical results of chapter 2 hold true. Equation (2.56) in particular needs to be checked and the validity of using a Gaussian as auto-covariance function has to be confirmed since the evaluation of the significance of any fluctuations about the mean relies critically on the ability to reliably calculate $\sigma_{\Delta\lambda}$. To this end 200 simulation runs were performed: For each run the spectra of 3 quasars were simulated simultaneously (the absorbers being distributed randomly) and $1 - D_A$ was measured as a function of wavelength and window size. The step size for both the position and the size of the window was chosen to be 2 pixels. The simulations were performed at a resolution of 2 Å and a signal to noise ratio per pixel of 20. For each point of the resulting 200 "transmission surfaces" the mean and the variance was calculated. Figure 2 shows the mean transmission surface and Figure 4 shows the corresponding σ-surface. In both cases the window size is given in pixels rather than in Mpc because the physical size depends on wavelength.

Both surfaces exhibit the expected behaviour: Figure 3 shows cross-sections through the mean transmission surface as a function of wavelength. Clearly, equation (2.48) describes the behaviour of $\langle 1 - D_A \rangle$ very well. The parameter B was determined by requiring

$$\langle 1 - D_A \rangle_{\mathrm{theo}} = \langle 1 - D_A \rangle_{\mathrm{measured}} \tag{4.1}$$

at the maximum window size: $B = 2.72 \times 10^{-3}$. The edge effect that was pointed out in section 2.2.1 is apparent in the upper panel of Figure 3. Figure 5 shows cross-sections through the σ-surface as functions of wavelength and window size. The window size is now given in proper Mpc. Again the theoretical calculations fit the simulations well. For this plot $q = 1.53$ and $\tilde{B} = 2^{\beta-1}\ B$. For both $\langle 1 - D_A \rangle$ and $\sigma_{\Delta\lambda}$ the input γ of 2.5 was used. Since σ is modelled well on *all* scales we can conclude that a Gaussian is a good approximation of the auto-covariance function of $e^{-\tau}$. In section 3.2.3 an upper limit of 10^{17} cm^{-2} was imposed on the column densities of absorbers. If *no* upper limit is imposed then (2.56) does *not* fit the simulations well anymore. Rather a small but non-vanishing term has to be added to $\gamma_{e^{-\tau}}$ which falls off only linearly out to at least 30 Å. This is because for $\log N > 17$ absorption lines are well saturated and their profiles resemble rectangles. Also, the width of a line in this column density regime is determined by N rather than the Doppler parameter b. Therefore, if we use (2.56) we must exclude large, damped absorption systems from the analysis. This is not a severe restriction since such systems are fairly rare.

4.2 Tpdf vs. line counting

In this section I will present the results from testing the new method of analysis. Its performance will be assessed and compared to the traditional line counting technique. It will be clearly demonstrated that the new method is able to detect large structures where line counting fails to do so. Both methods were applied to the two clustering scenarios described in the previous chapter.

All simulations in this section were carried out at a resolution of 2 Å and a signal to noise ratio per pixel of 20. In each case 5 spectra of existing QSOs were simulated. They range in redshift from 2.63 to 2.87 and the proper separations among them range from 4 to 19 h_{100}^{-1} Mpc.

4.2.1 GQED

For this simulation the clustering parameter b was chosen to be 0.4 for illustrative purposes (today's value of b for galaxies ≈ 0.75). Figure 6 shows the overlapping part of the regions between Lyα and Lyβ emission lines of the five simulated spectra. Although there are some stretches that seem fairly devoid of absorption lines, the presence of clustering is not obvious. To confirm that clustering is indeed present, Figure 7 shows the three dimensional two-point correlation function of the specific population of absorbers that created the spectra of Figure 6. It was measured by selecting a random subsample of $N_{\rm sub}$ absorbers, distributing a second, *random* population of $N_{\rm rand}$ objects and calculating

$$\xi(r) = \frac{N_{\rm AA}(r)}{kN_{\rm AR}(r)} - 1, \tag{4.2}$$

where

$$k = \frac{N_{\rm sub}\,(N_{\rm sub} - 1)/2}{N_{\rm sub}\,N_{\rm rand}} \tag{4.3}$$

and $N_{\rm AA}$ ($N_{\rm AR}$) is the number of absorber-absorber (absorber-random) pairs with separation r (Drinkwater 1987). The dashed histogram is the 1σ error which is given by $1/\sqrt{N_{\rm AR}}$. There is a large excess of pairs in the first bin which is expected since clusters were chosen to have a radius of 1 Mpc (see section 3.2.2).

Similarly, one can construct the one dimensional two-point correlation function along the line of sight by counting the number of pairs of absorption lines at a given separation, dividing by the number of expected pairs (which can be calculated in the one dimensional case) and subtracting one. The separation is usually given in velocity space. Given the true positions of all the lines in the spectra of Figure 6 this procedure gives a similar clustering signal as obtained before. For real data however, the positions of the absorption lines have to be determined by detailed fitting of every absorption feature in the observed spectra. This process has been simulated here by transforming the "true" or input list of absorption lines into an "observed" one:

1. Only lines with $N > 5 \times 10^{12}$ cm^{-2} are used, thus allowing for the limited signal to noise ratio.

2. All lines within one FWHM of each other (or one typical line width; whichever is larger) are blended into a single "line" with a redshift equal to the average redshift of its components.

This simple procedure of generating "observed" line lists is known to be a fairly good approximation of reality (Fernández-Soto et al. 1996). Figure 8 shows the line of sight two-point correlation function averaged over the five spectra. There is *no* indication of clustering. An average over any subset of the five spectra gives the same result. In contrast, Figure 9 shows the transmission surface of the five spectra. At each point, $\langle 1 - D_A \rangle$ was subtracted and the result was divided by $\sigma_{\Delta\lambda}$ using the values of B, $\tilde{B}$, and q determined in the previous section. There are two $\sim 4\sigma$ events, one at ~ 4020 Å and another one at ~ 4380 Å. Going back to Figure 6 we see that at both these positions there is fairly strong absorption in the first two spectra. In both cases the size of the overdensity is given as 2 Mpc which corresponds well to the size of clusters, thus indicating that the excess absorption at these positions is due to one or several clusters and not just a random conglomeration of unclustered absorbers. Indeed, the absorption feature at 4380 Å e.g. is caused by three different clusters: Two clusters at redshifts 2.6 and 2.61 with 5 and 4 members respectively in the first spectrum and a cluster with 6 members at redshift 2.6 in the second spectrum. Thus the analysis has also correctly determined the redshift of the clusters. Also, the lack of lines around 4180 Å in the third and fifth spectra has been classified as a $\sim 3\sigma$ void. Thus the transmission surface properly reveals structure which has remained undetected using the two-point correlation function.

4.2.2 Walls

Figures 10 – 13 show the result of the same analysis as described above for the case of a single wall of absorbers extending across all sightlines and having a thickness of 7.5 h_{100}^{-1} Mpc proper at redshift 2.48 (26 h_{100}^{-1} Mpc comoving). The number density of absorbers inside the wall is 1.8 times higher than outside. Again a visual inspection of the spectra does not give any indication of structure. Although the signal in the true, three dimensional two-point correlation function is weak, it is definitely significant since the first eight consecutive bins are all above the 1σ level (Figure 11). As before, the line of sight two-point correlation function shows no significant signal when computed using the "observed" line positions and averaged over all five spectra (Figure 12) or any subset thereof. In this case a *cross*-correlation of absorption lines in pairs of spectra was also performed, but no combination revealed any other result. The transmission surface however, has a very characteristic appearance and the presence of the wall is strikingly obvious as a $\sim 4.2\sigma$ event (Figure 13). Figure 14 shows cross-sections through the transmission surface and the maximum is seen to occur at 4233 Å and 7.5 h_{100}^{-1} Mpc which is notably close to the wall's true size and position. As before, the transmission surface has reliably detected the presence of structure in the spectra which has eluded the commonly used line counting method.

4.3 Close double lines of sight

This section has no direct connection with the previous ones and should be viewed as an aside.

The study of coincident and anticoincident absorption lines in the spectra of closely spaced QSOs can put upper limits on the sizes of Lyα clouds and constrains the possible geometries (Sargent et al. 1982, Dinshaw et al. 1994, Crotts & Fang 1997). One technique to discriminate between different models of how the gas is distributed in an absorber is to study the correlation of column densities of coincident lines. Charlton et al. (1995) have used simulations similar to the ones presented here to demonstrate the major characteristics displayed by different model geometries. As described in chapter 3 they have also used a smooth column density distribution $N(r)$. It is clear that the $N_{\rm A}$-$N_{\rm B}$ correlation of coincident lines in two lines of sight, A and B, will depend critically on R, the ratio of line of sight separation to the size of absorbers. Charlton et al. assumed R to be constant for a given pair of lines of sight. Here, I show the results for

$$R(z) = \frac{d(z)}{r_0(z)}, \tag{4.4}$$

where $d(z)$ and $r_0(z)$ are given by (2.8) and (3.6) respectively. The lower panel of Figure 15 shows $R(z)$. In this plot the angular separation between the two lines of sight was taken to be $1'30''$. From the upper panels of Figure 15 we see how the correlation weakens for widening angular separation of the lines of sight. The "density ridges" astride the $N_A = N_B$ correlation line that were pointed out by Charlton et al. (compare their Figure 1) are clearly visible although somewhat weakened by the varying R. Also, the sharp, curved edge which delimits the points of the scatter plot towards the upper right corner in the case of constant R is lost.

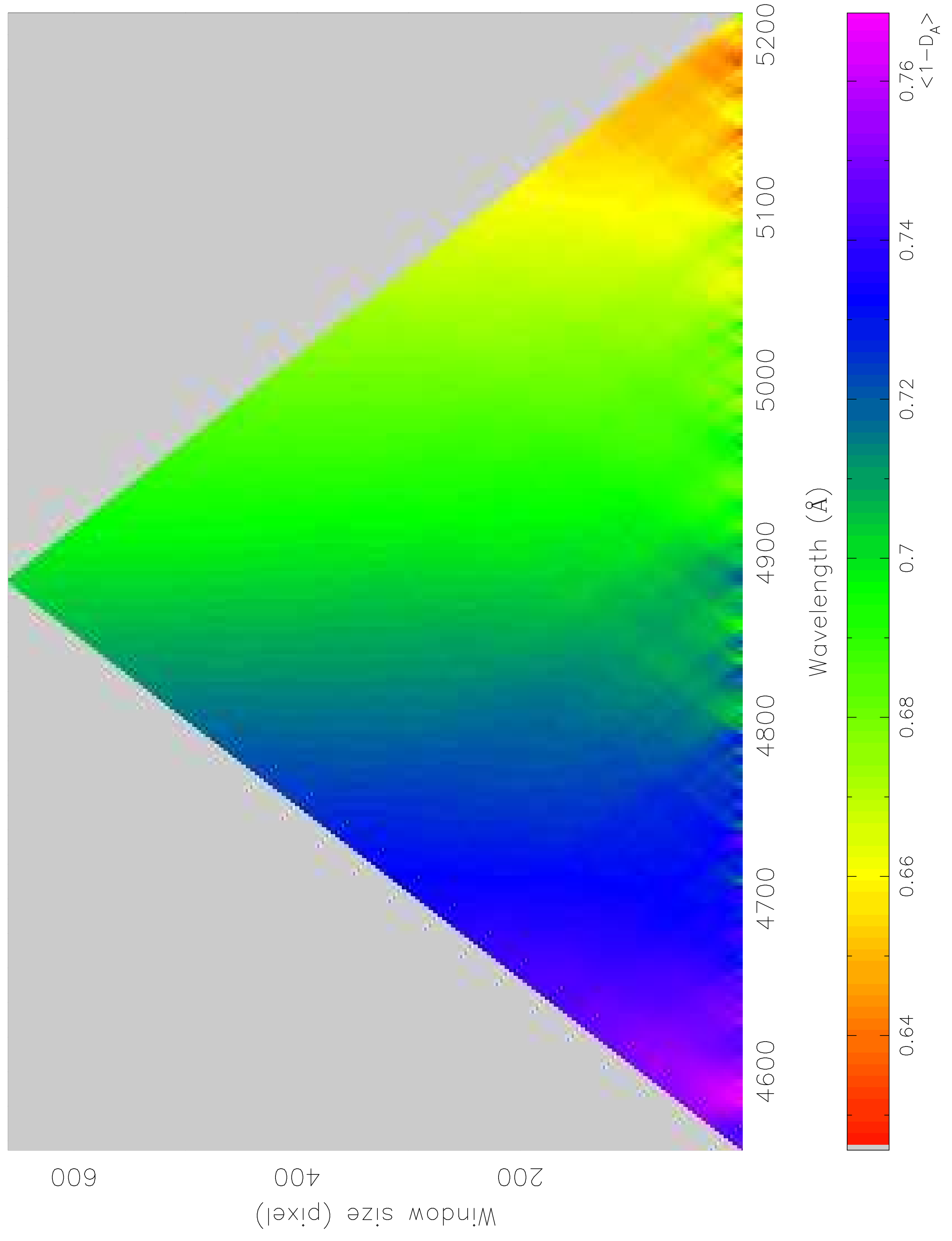

Fig. 2.— The mean transmission surface of 200 simulations.

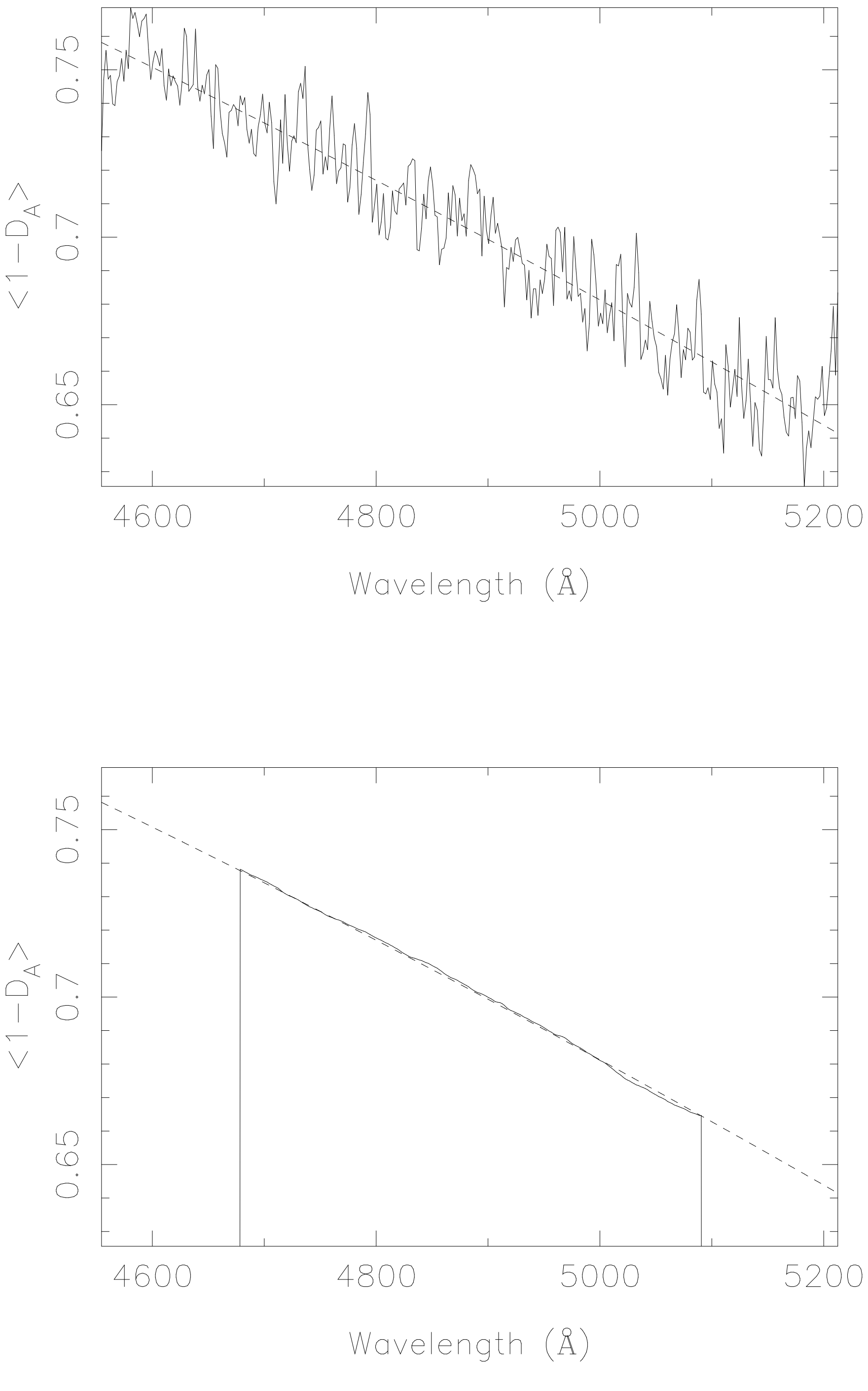

Fig. 3.— Cross-sections of the mean transmission surface at window size = 1 pixel (upper panel) and at 247 pixels (lower panel). Dashed lines are theoretical curves.

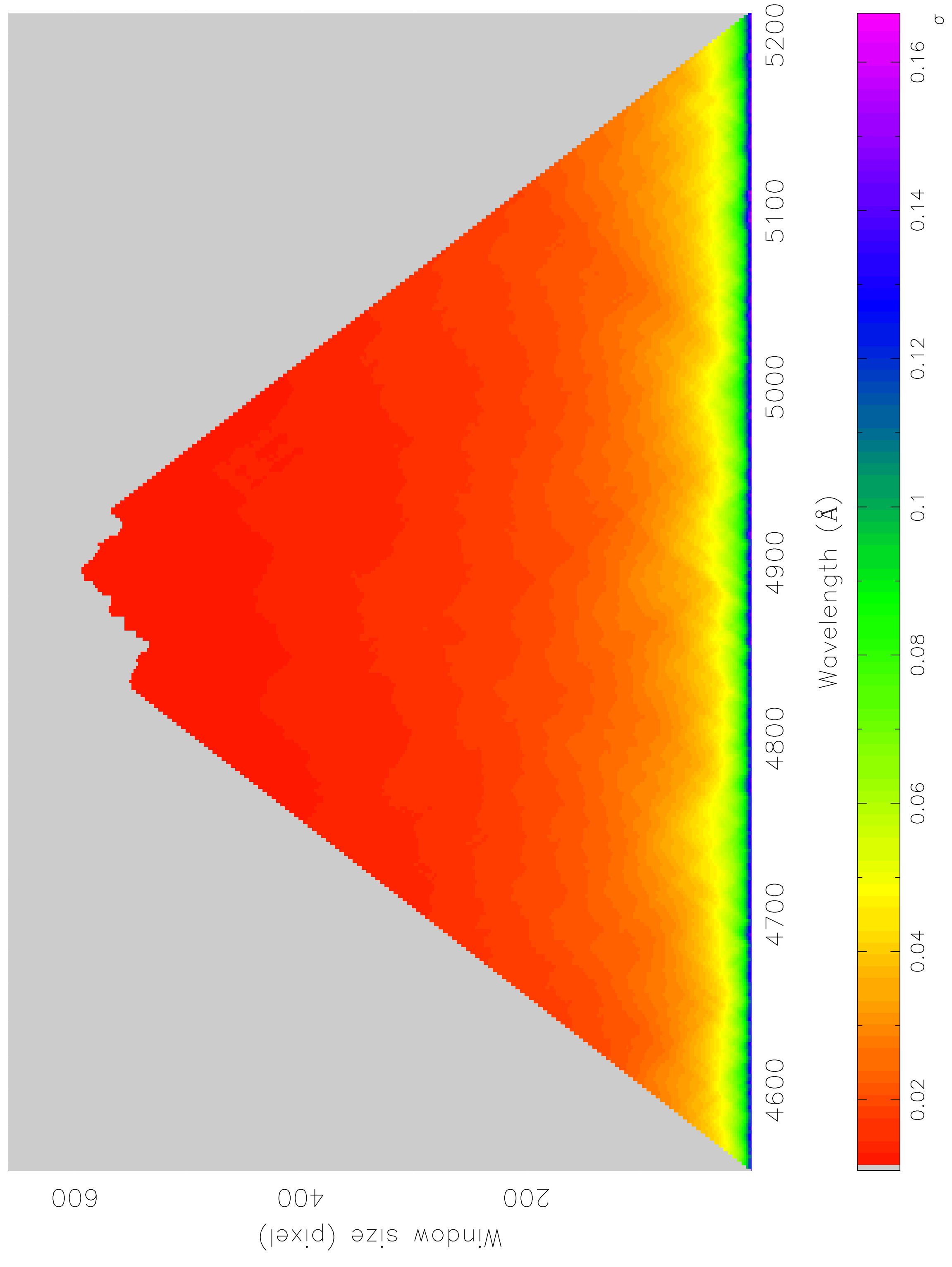

Fig. 4.— The sigma surface of 200 simulations.

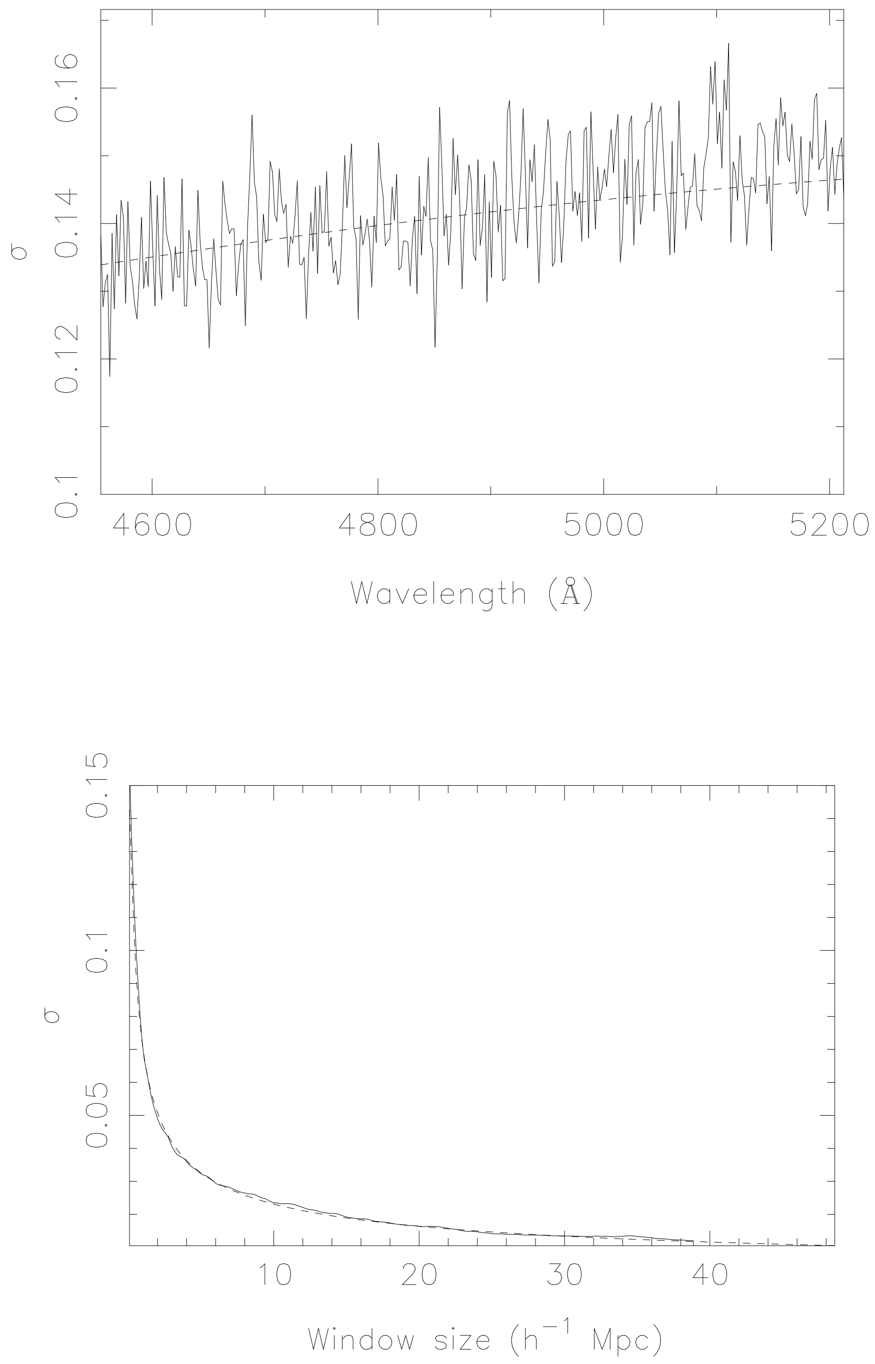

Fig. 5.— Cross-sections of the sigma surface as a function of wavelength at window size = 1 pixel (upper panel) and as a function of window size at 4950 Å (lower panel). Dashed lines are theoretical curves.

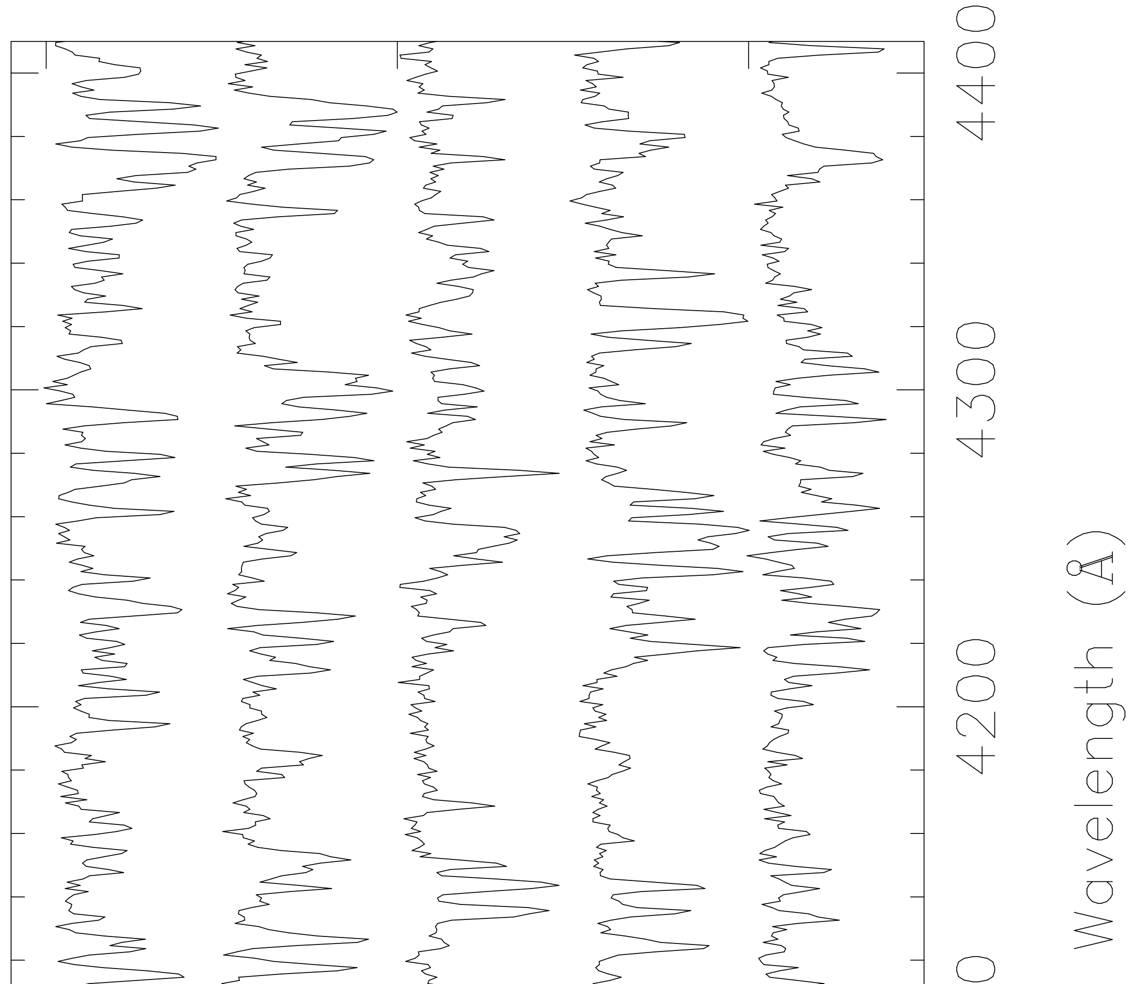

Fig. 6.— Simulated spectra. Absorbers are clustered with $b = 0.4$.

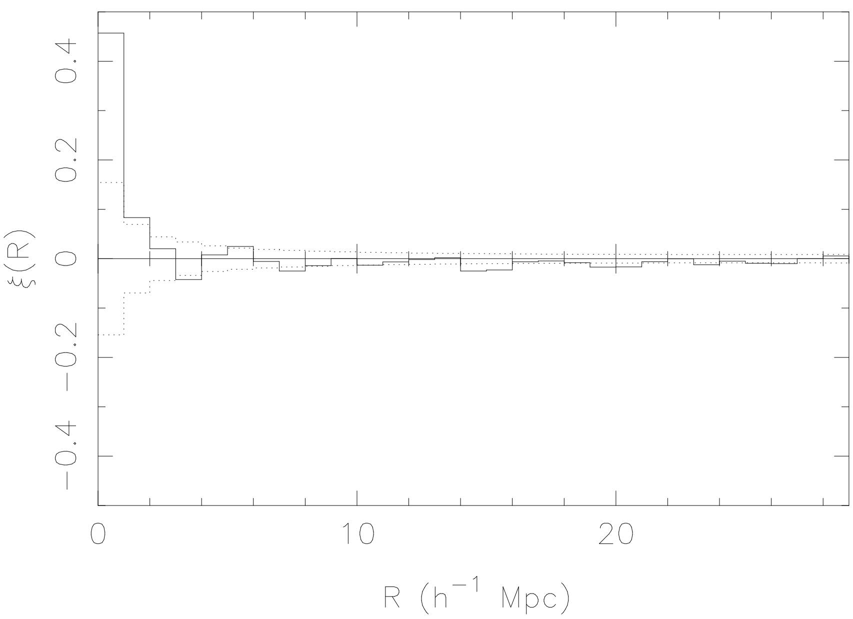

Fig. 7.— Two-point correlation function of absorbing galaxies as derived from actual RA, DEC, and z for the GQED scenario.

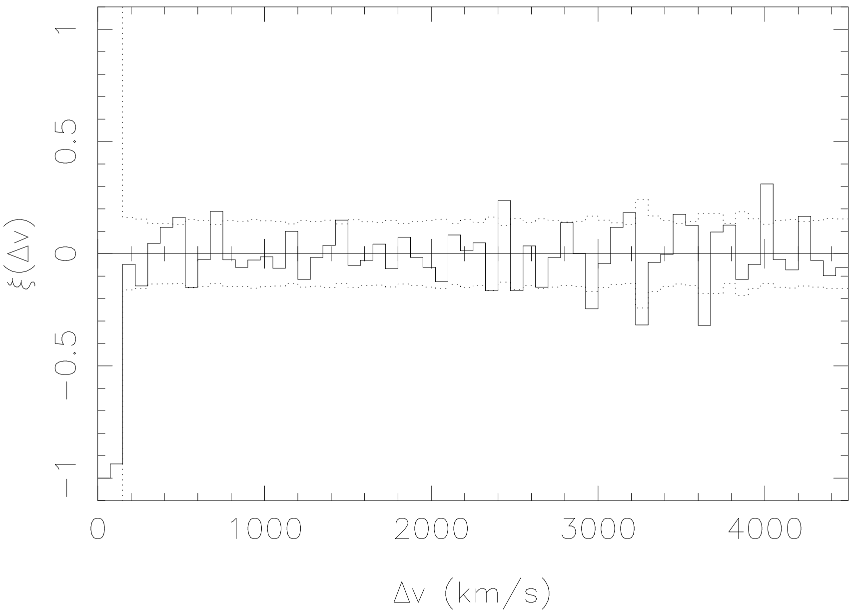

Fig. 8.— Line of sight two-point correlation function as computed from "observed" positions of absorption lines, allowing for line blending (see text) for the GQED scenario. The first two bins of the error array should be ignored.

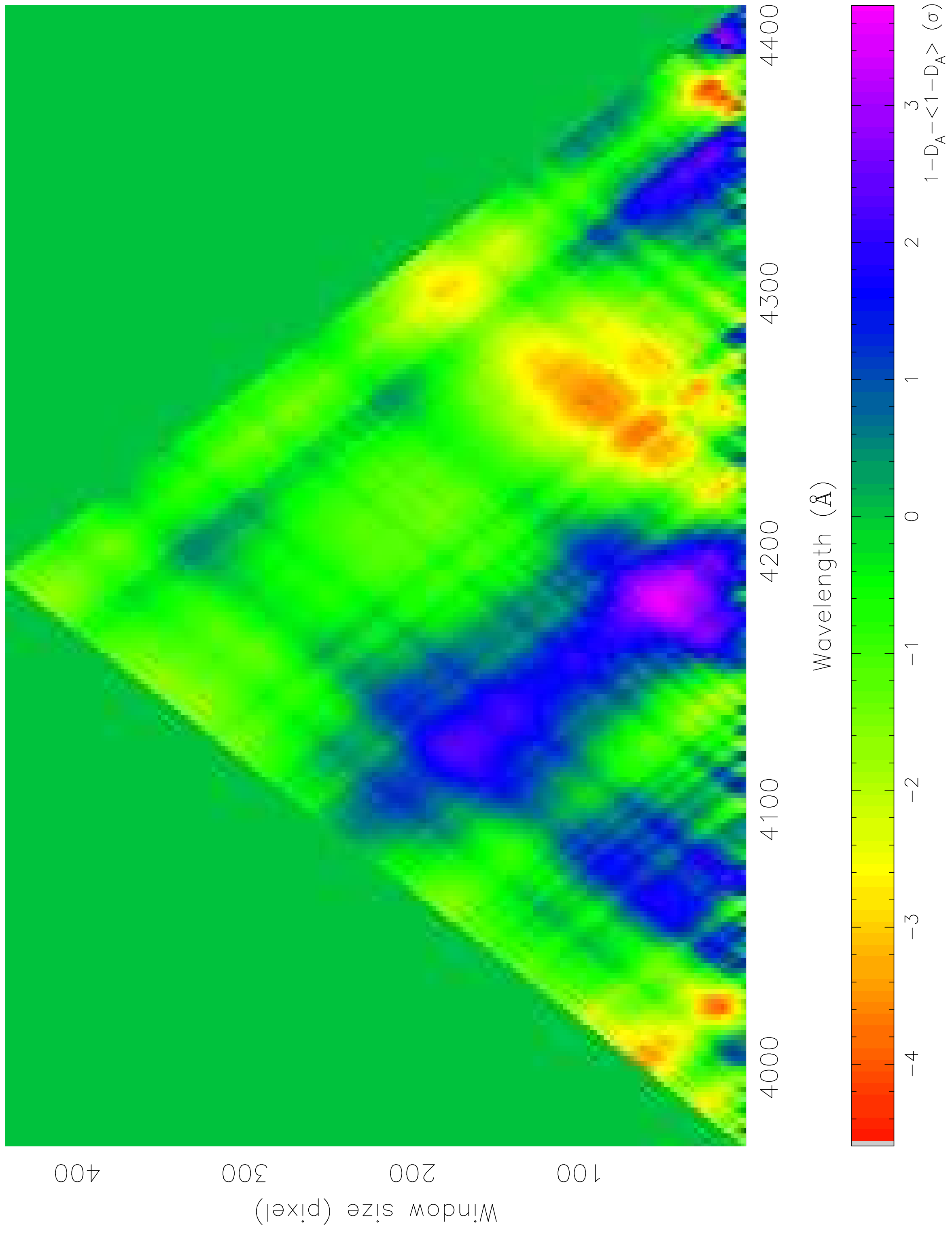

Fig. 9.— Transmission surface of five simulated spectra for the GQED clustering scenario.

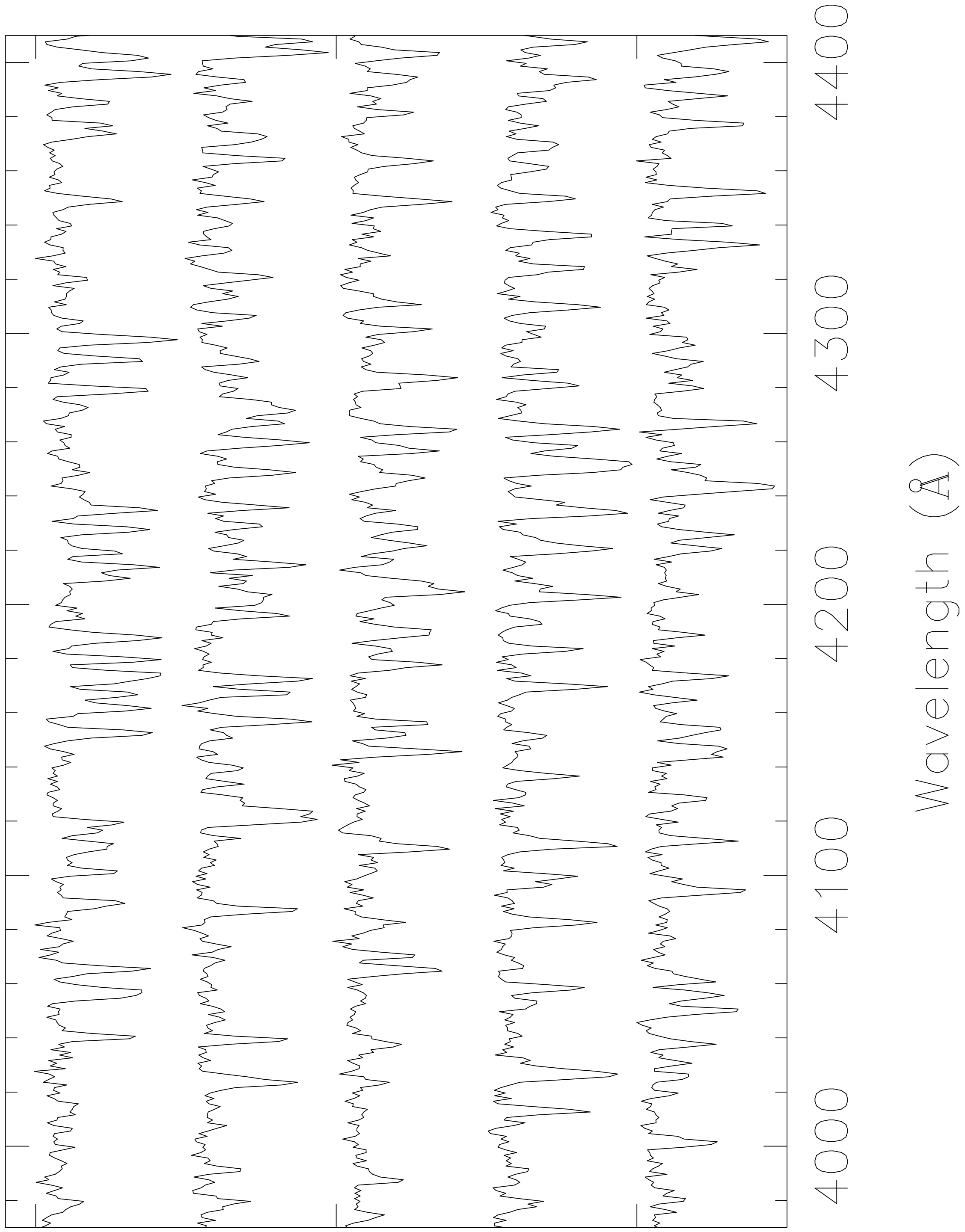

Fig. 10.— Simulated spectra. A “wall” of absorbers of overdensity 1.8 and width 68 Å is located at 4226 Å.

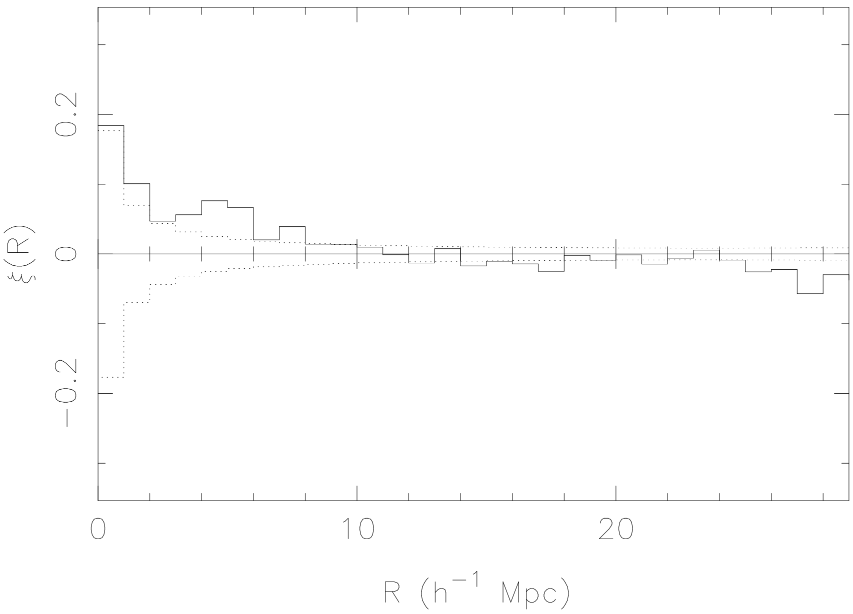

Fig. 11.— Two-point correlation function of absorbing galaxies as derived from actual RA, DEC, and z for the case of a wall of galaxies.

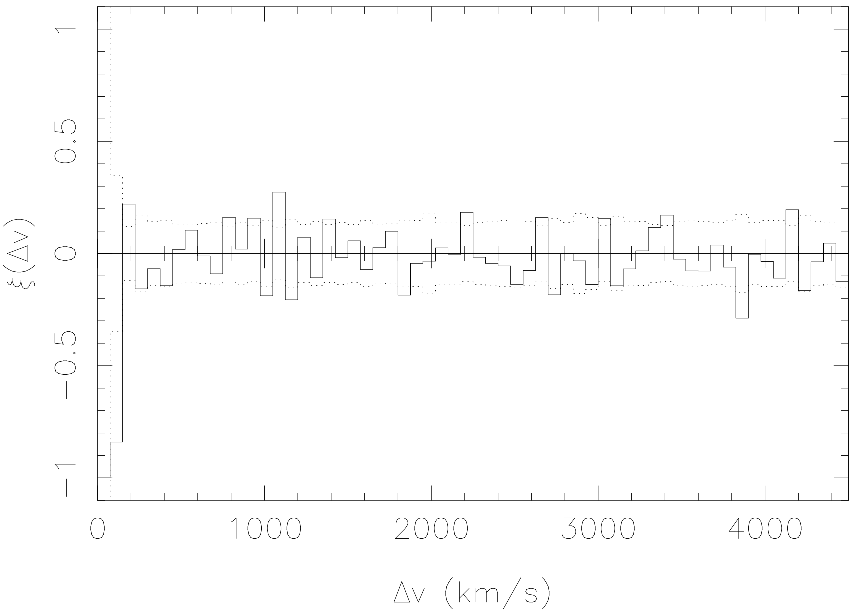

Fig. 12.— Line of sight two-point correlation function as computed from "observed" positions of absorption lines, allowing for line blending (see text) for the case of a wall of galaxies. The first two bins of the error array should be ignored.

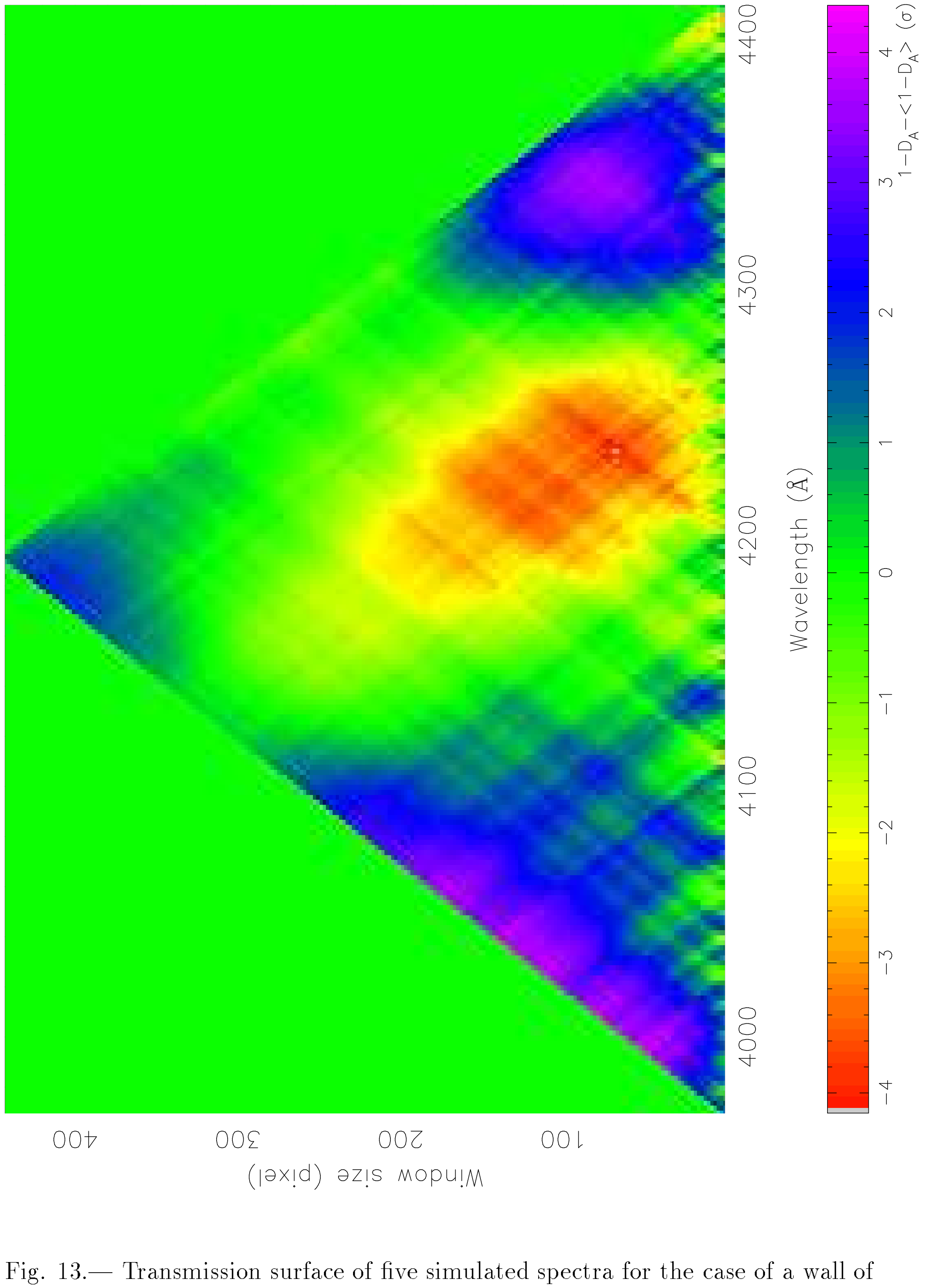

Fig. 13.— Transmission surface of five simulated spectra for the case of a wall of absorbers.

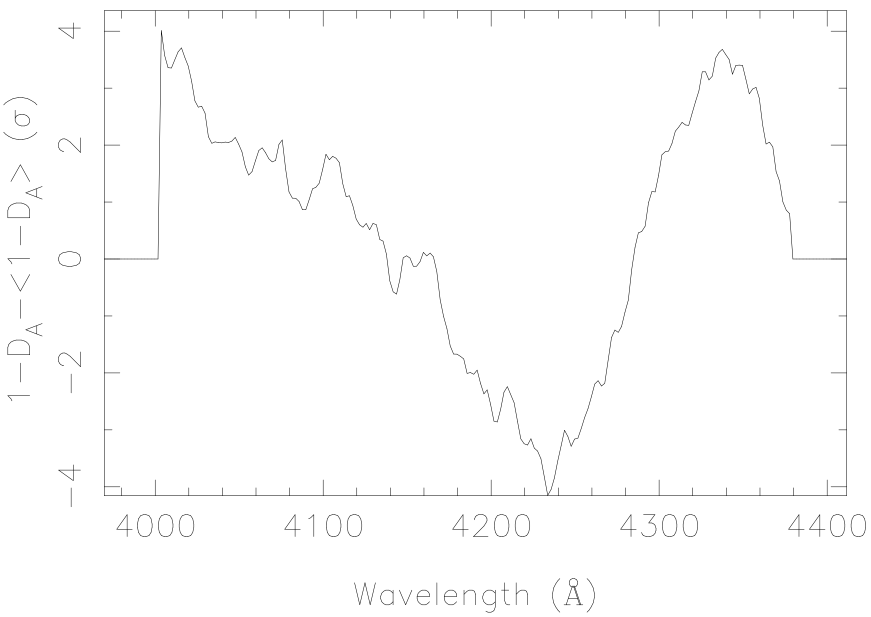

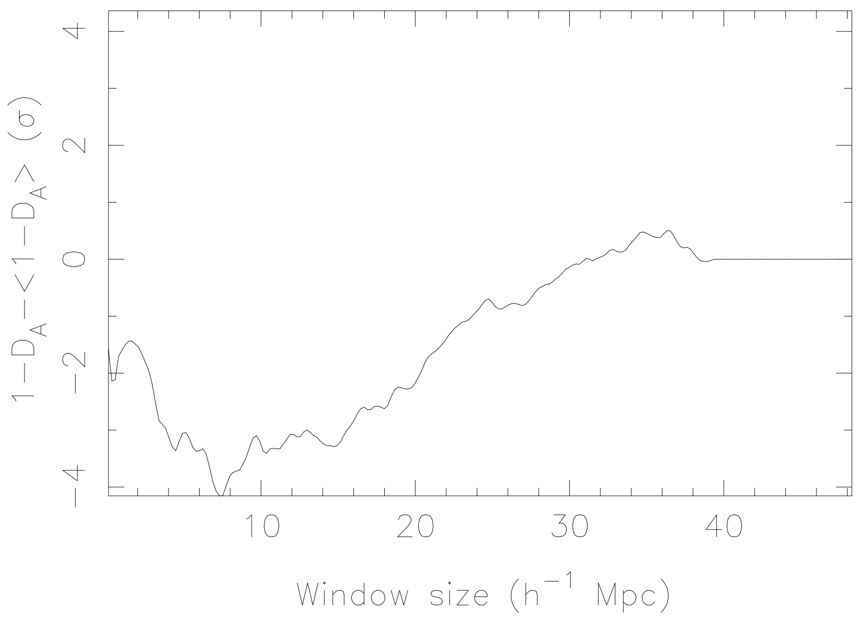

Fig. 14.— Cross-sections of the transmission surface of Figure 13

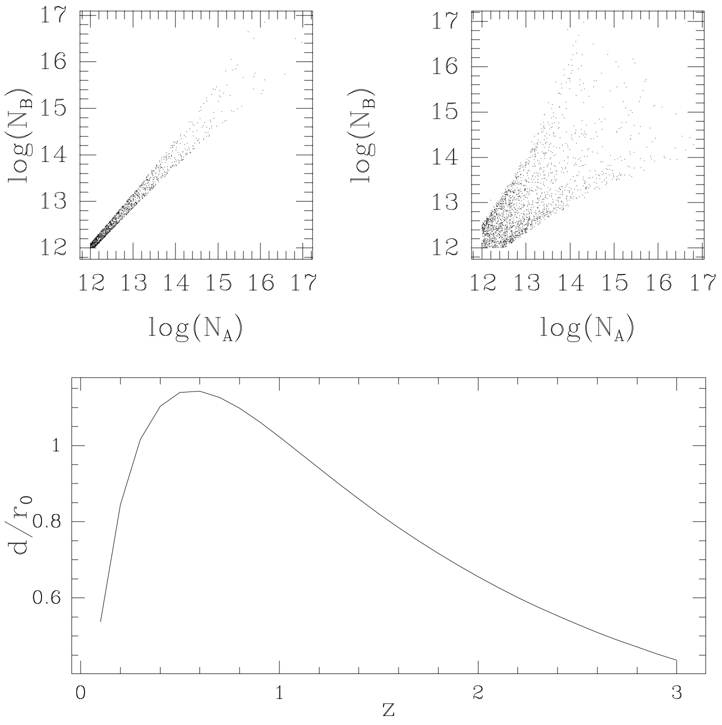

Fig. 15.— Correlation of column densities of coincident lines. Upper left panel shows the case of 36" separation, upper right panel shows 1'30" separation and $z_{\rm em} = 3$ in both cases. Lower panel shows ratio of proper separation of sightlines to r_0.

Chapter 5

The Data

In this chapter I will briefly describe the data that was analysed using the new method proposed in this work. The data was kindly made available to me by Gerard Williger. The observations were made on the CTIO 4 m telescope using the Argus multifibre spectrograph. The instrumental resolution was ~ 2 Å and the signal to noise ratio per pixel reached up to 40 per 1 Å pixel. For a complete description of the observations and the reduction process see Williger et al. (1996, 1997). In all, spectra of 25 QSOs in the South Galactic Pole field were obtained.

Williger et al. (1997) have analysed the spectra of 10 QSOs using the traditional line counting procedure and report correlations on the scale of 36 h^{-1} Mpc comoving *in the plane of the sky* at the 3.8σ level while they see no significant correlation *along the line of sight*. Thus this data presents an excellent opportunity to test the new method and hopefully detect the structures responsible for the signal in the two-point correlation function.

I have selected eight QSOs for detailed studies. Their positions and redshifts are given in Table 1. They all lie within a $\sim 1°$ field (see Figure 1) which corresponds to a maximal proper separation of $\sim 14\ h_{100}^{-1}$ Mpc ($q_0 = 1/2$). The distribution in redshift space is shown in Figure 2.

Usually, continua shortward of Lyα emission are obtained by fitting multiple splines or other high order polynomials to regions that appear to be free of absorption. Because of the abundant absorption by Lyα clouds shortward of Lyα emission it is very difficult to fit a continuum in this region. The continuum fits

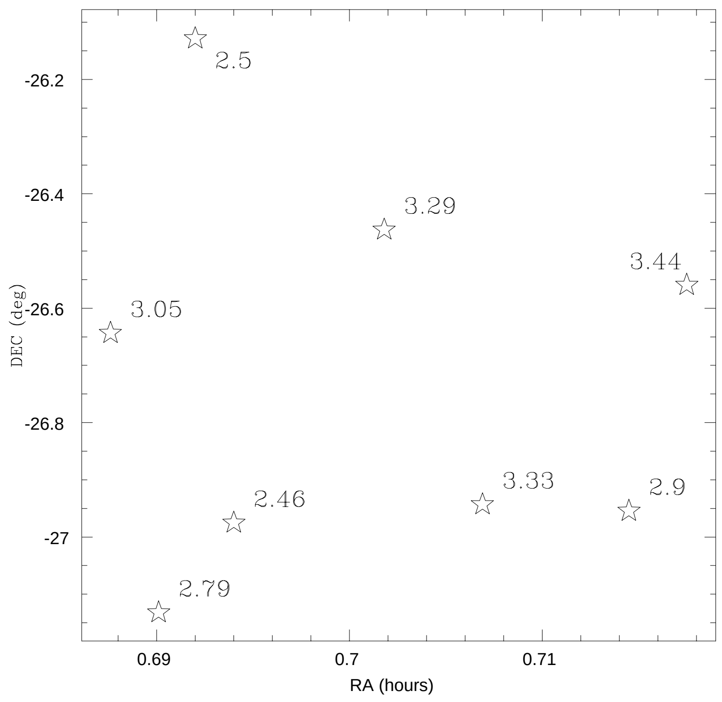

Fig. 1.— Observed QSOs in the SGP field

were also obtained from Williger. In figure 3 the normalised spectra shortward of Lyα emission are shown. In almost all spectra we can see some residual "waviness" longward of Lyα emission, probably due to imprecise fitting of the Lyα and NV emission lines. The general problem of accurately determining the continuum must be kept in mind when analysing the data and assessing the significance of any signal since this ignorance of the precise placement of the continuum was not taken into account in either the theoretical calculations nor the simulations. Unfortunately, it has not been possible to obtain more precise continuum fits due to the short time the data has been available to me. For the same reason I have not been able to remove metal lines which contaminate the Lyα forest. Since metal lines are known to cluster (Williger et al. 1996) it is important to exclude the relevant spectral regions from the analysis. This will be treated in detail in a forthcoming publication.

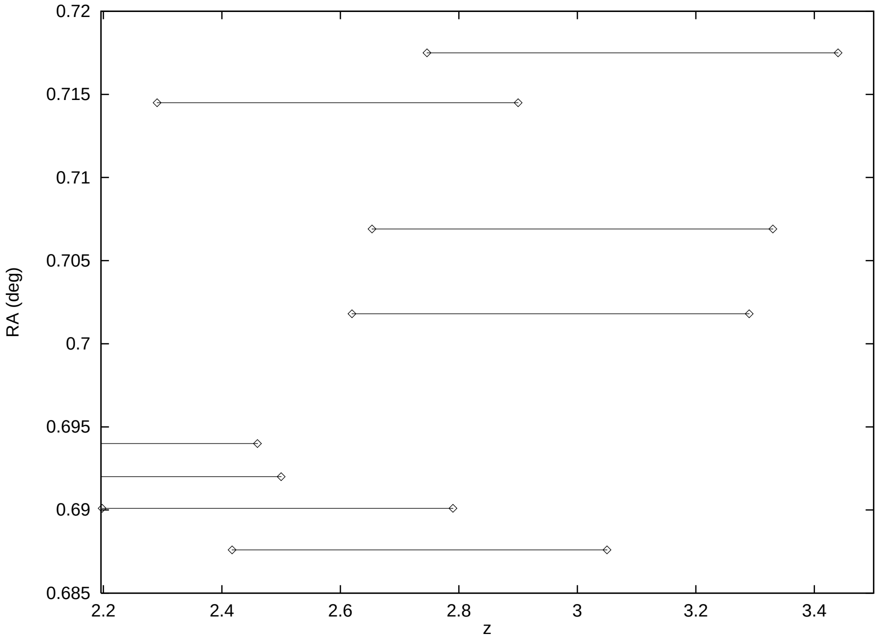

Fig. 2.— Observed QSOs in the RA-z plane. The lines show the wavelength ranges between Lyα and Lyβ emission lines.

It is important to stress the uniformity of the data in terms of instrumental setup and reduction process.

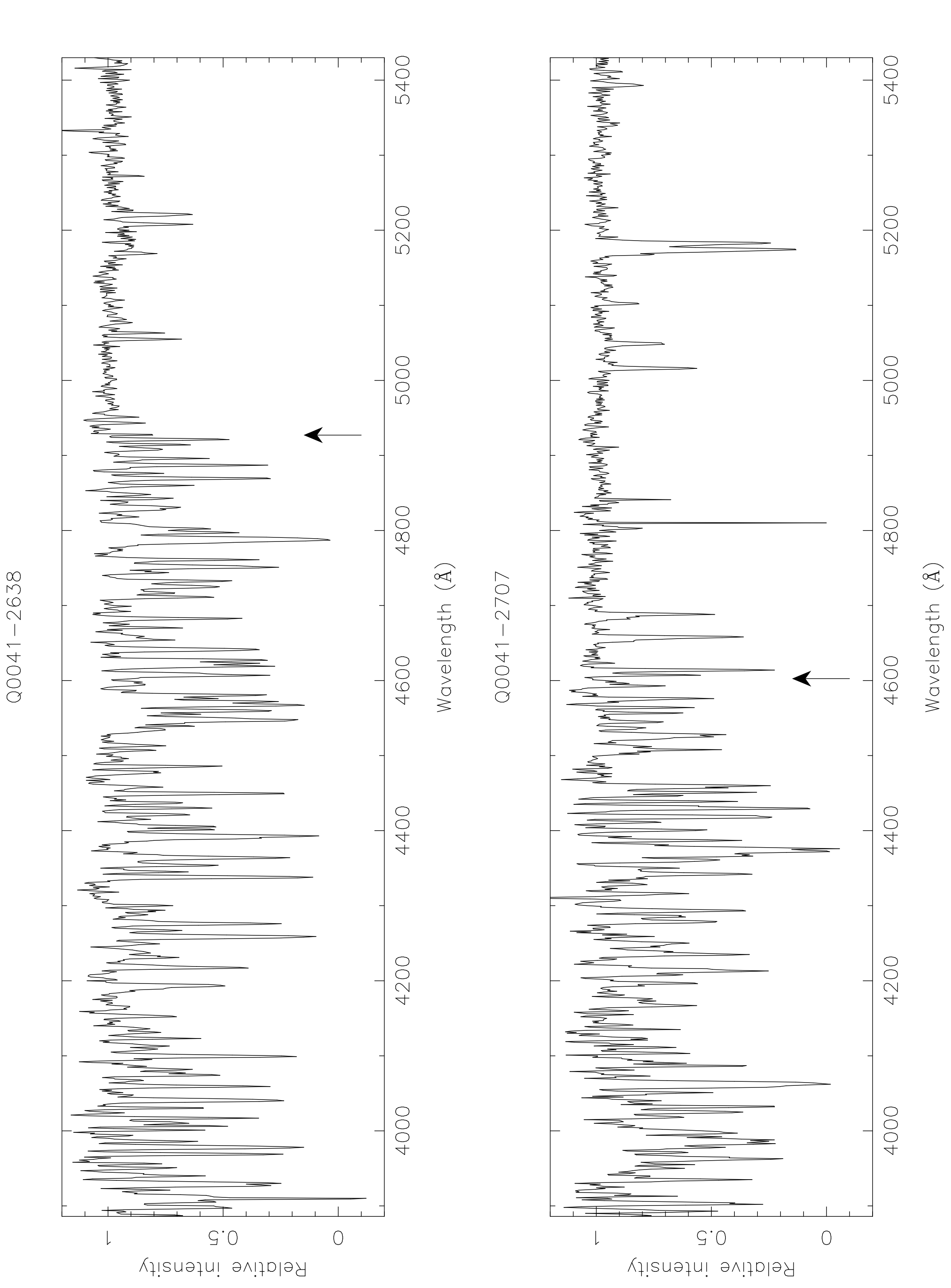

Fig. 3.— Normalised QSO spectra. Arrows indicate the position of the Lyα emission line.

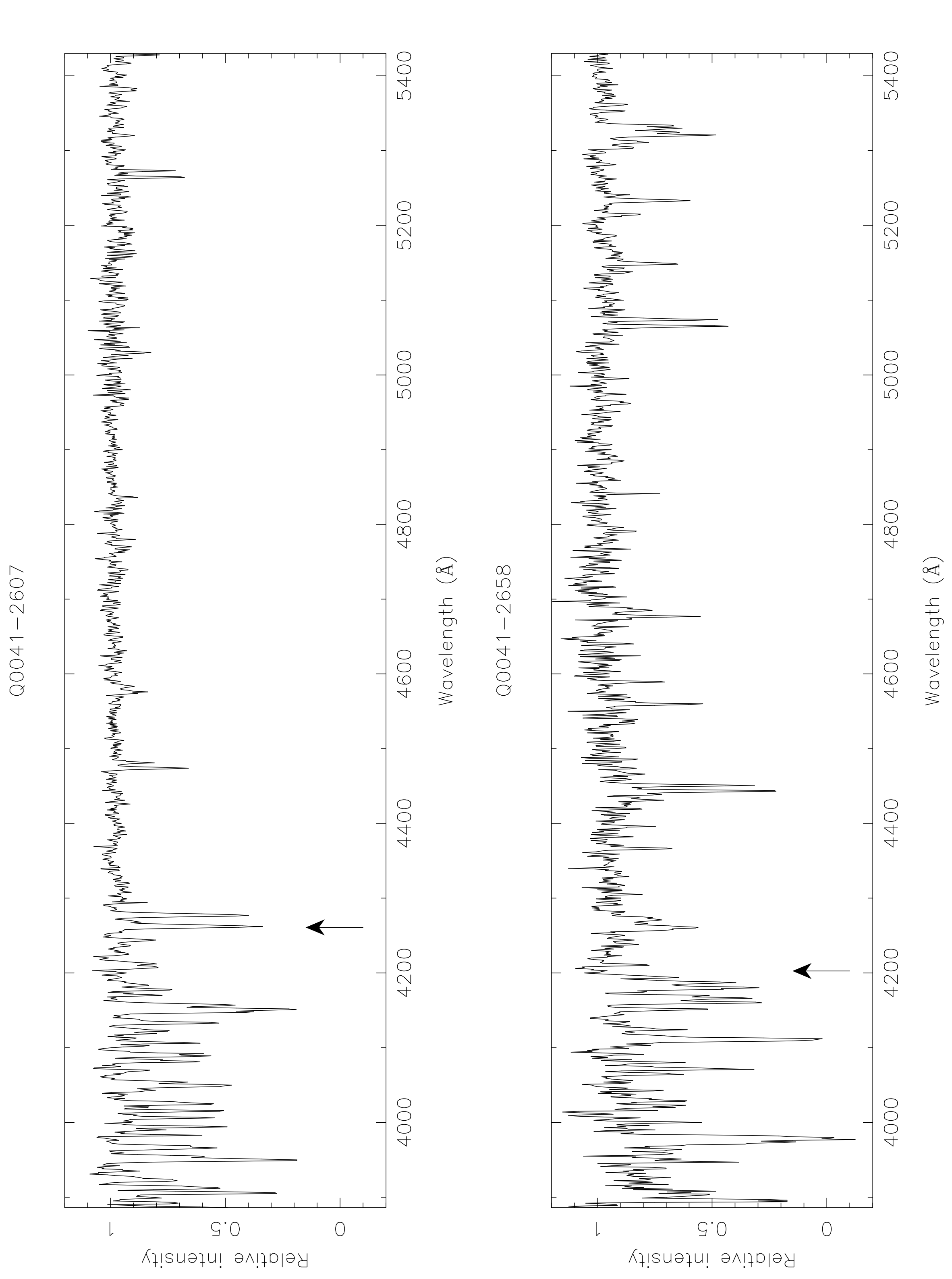

Fig. 3.— continued

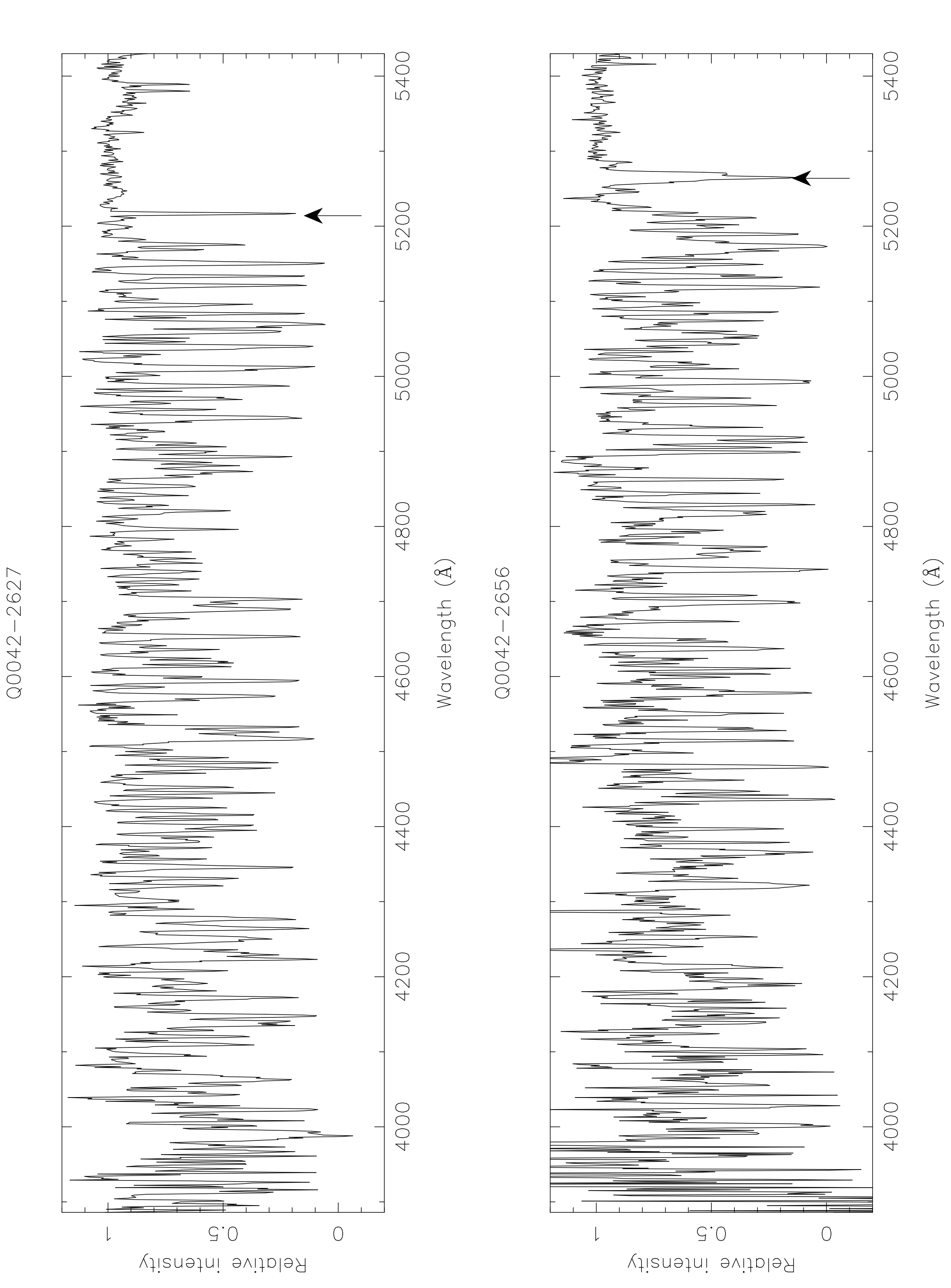

Fig. 3.— continued

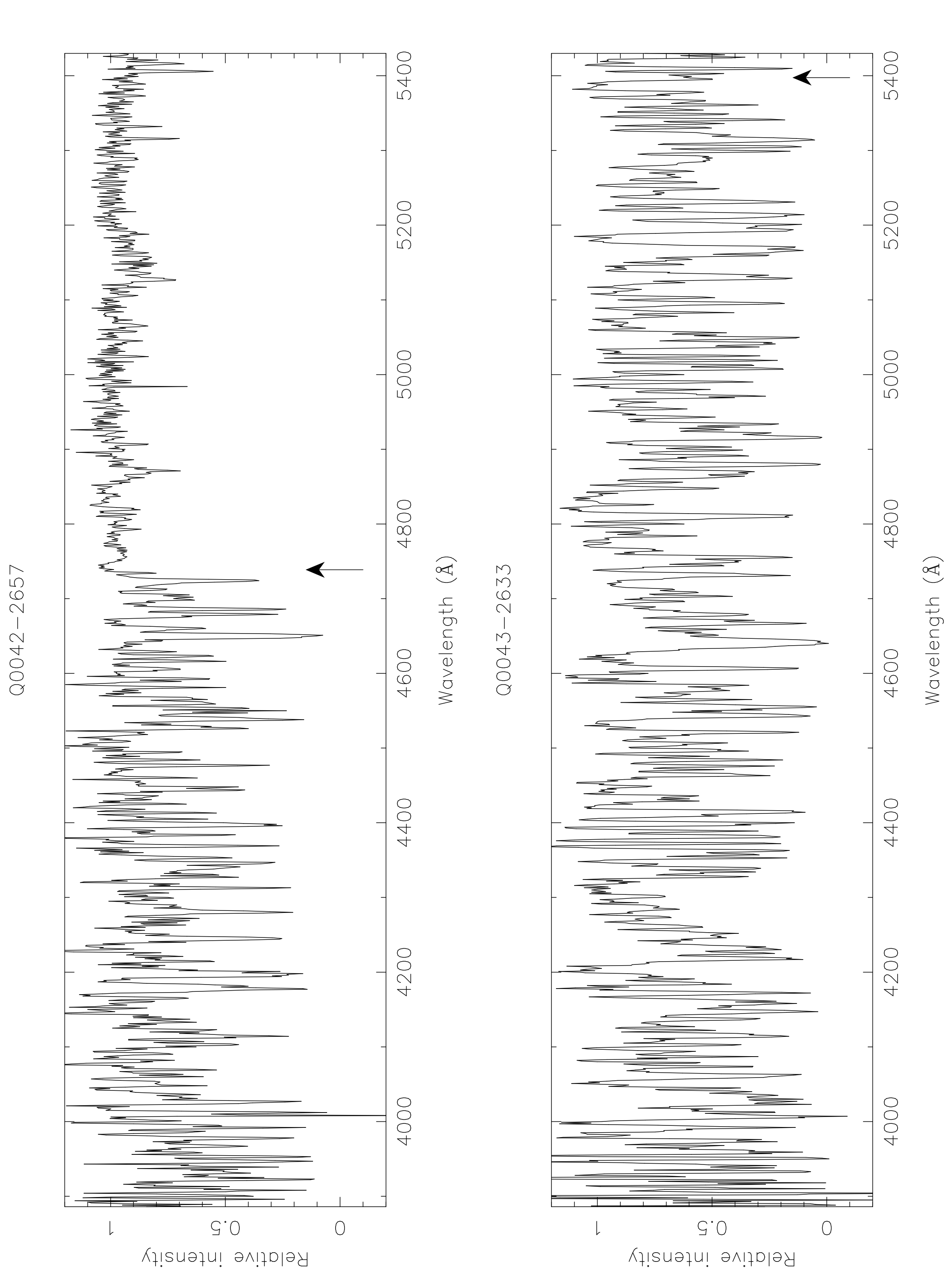

Fig. 3.— continued

Table 1. Observed QSOs

Object	RA_{1950} h m s	DEC_{1950} $\circ$ $'$ $''$	z_{em}
Q0041 − 2607	00 41 31.11	−26 07 41.7	2.505
Q0041 − 2638	00 41 15.19	−26 38 35.9	3.053
Q0041 − 2658	00 41 38.38	−26 58 30.0	2.457
Q0041 − 2707	00 41 24.38	−27 07 54.3	2.786
Q0042 − 2627	00 42 06.42	−26 27 45.3	3.289
Q0042 − 2656	00 42 24.89	−26 56 34.4	3.33
Q0042 − 2657	00 42 52.29	−26 57 15.3	2.898
Q0043 − 2633	00 43 03.10	−26 33 33.6	3.44

Chapter 6

Results from the Data

The spectra of the eight quasars presented in chapter 5 were analysed using the new method. For each spectrum, the region within 3000 km/s from the quasar's redshift was excluded from the analysis in order to avoid the proximity effect (Webb & Larsen 1987) (see also section 2.2.1). Also, the first 50 pixels from each spectrum were excluded because the data in that region appeared to be very noisy which is probably due to atmospheric effects and a lack of sensitivity of the instrument/telescope at the blue end of the spectrum. Thus, the total wavelength coverage extends from 3886 Å to 5342 Å which corresponds to 2.20 – 3.39 in redshift space.

The parameters γ, B, $\tilde{B}$, and q that are needed for computing $\langle 1 - D_A \rangle$ and $\sigma_{\Delta\lambda}$ are determined in the following way: γ was adopted from Williger et al. (1997) who found $\gamma = 2.5 \pm 0.8$. We shall see later that indeed this value fits the data well. From the simulations it was found that $q = 1.53$ and $\tilde{B} = 2^{\beta-1}B$ provided a good fit, so these values will be retained. As pointed out in chapter 2, B essentially determines the overall normalisation so one would like to use the entire data set for its determination. Towards this end a B value was calculated for each spectrum *individually* according to

$$B_i = -\ln(1 - D_A)_i \left(\frac{\lambda_\alpha}{\lambda_i}\right)^{\gamma+1}, \tag{6.1}$$

where λ_i denotes the central wavelength of i-th spectrum[1] and $(1 - D_A)_i$ is taken over the entire spectrum (the value at the very top of the transmission "pyramid" of the i-th spectrum). Since only about half of the spectra of Q0041-2607 and Q0041-2658 are included in the wavelength region covered by the observations their B_i values will be disregarded in the following. The arithmetic mean of the B_i provides an estimate of the universal value of B and gives 2.69×10^{-3}. This is in fair agreement with the value measured from the simulations in section 4.1 which is not too surprising since these simulations were run with the same number density of absorbers that was needed to reproduce the appearance of the observed spectra. However, using this value of B to calculate the theoretical expectation value $\langle 1 - D_A \rangle$ and $\sigma_{\Delta\lambda}$ we find that three of the six $(1 - D_A)_i$ lie more than 2σ away from their expected values where we would expect only 0.3 (assuming Gaussian statistics). This behaviour was *not* encountered in the simulations and must be discussed in more detail.

In principle, there are three possible explanations:

1. Any or all of the parameters of the cloud distribution function (3.7) may evolve with redshift. This hypothesis is rejected on the grounds that there is no B-z correlation.

2. The effect is indeed due to clustering. The large window size seems to indicate an enormous clustering scale. However, although very large windows are used to compute the $(1 - D_A)_i$ their values are still sensitive to *small* scale clustering because the Fourier transform of a top-hat function has fairly large side lobes. Nevertheless, if clustering were indeed the cause of the B_i fluctuations then one would expect $\Delta B_{ij} = |B_i - B_j|$ to correlate with the angular separation of the i-th and j-th sightline. Figure 1 shows the scatter diagram of ΔB_{ij} vs. angular separation and there is indeed a marginal indication of correlation. If we accept this explanation then instead of simply dividing $\sigma^2_{\Delta\lambda}$ by $N_{\rm spec}$ as suggested in chapter 2 we must

[1] From now on the term "spectrum" refers to the region between Lyα and Lyβ emission lines, excluding the part effected by the proximity effect.

calculate

$$\frac{1}{N_{\rm spec}^2}\sum_{i=1}^{6}(\sigma_{\Delta\lambda}^2)_i \tag{6.2}$$

(neglecting the correlation across sightlines). This possibility remains to be explored in more detail in the future.

3. It is more likely though, that the unusually large variance in the B_i arises from an error in the zeroth and first order components of the continuum fit. We shall adopt this explanation as the correct one.

The following strategy is an attempt to correct for this effect: at a given point in the window size – window position plane $(1 - D_A - \langle 1 - D_A \rangle)_i$ is computed for the i-th spectrum, where $\langle 1 - D_A \rangle$ is calculated using B_i. This value is then averaged over all spectra that entirely contain the window. Finally, the average is divided by $\sigma_{\Delta\lambda} / \sqrt{N_{\rm spec}}$, where $N_{\rm spec}$ is the number of spectra used and $\sigma_{\Delta\lambda}$ is calculated using the *universal* value of B. This technique avoids over- or underestimating $\sigma_{\Delta\lambda}$ because of a "wrong" mean transmission level due to an inaccurate continuum fit. It must be kept in mind that this procedure only corrects for errors in the zeroth or first order component of the continuum fit and that erroneous *small scale* behaviour may still lead to false detections.

Figure 2 shows the result of the analysis described above. The success in removing the effect of the artificially introduced fluctuations of the B_i is demonstrated by the fact that most of the "edges" of the individual transmission "pyramids" are virtually invisible. By inspecting Figure 3 which shows the cross-section of the transmission surface at window size = 1 pixel, we also find that $\gamma = 2.5$ fits the data well since there is no residual overall dependency on wavelength. Figure 2 reveals some interesting features. There is a 5.3σ overdensity at 3974 Å and at a size of 6.8 h_{100}^{-1} proper Mpc which corresponds to 22.2 h_{100}^{-1} comoving Mpc. This signal is caused by the spectra of Q0041-2707 and Q0041-2658. Both of these spectra (but especially Q0041-2707) exhibit strong absorption at ~ 3980 Å and the sightlines are only separated by 2.4 h_{100}^{-1} proper Mpc at the redshift of the feature of 2.27. Although this overdensity may seem close to the edge of the data coverage, it must be remembered that the first 50 Å have already been excluded from the analysis and a close inspection of the spectra does not reveal any irregularities. Even if we allow for a 5 percent error in the continuum fit at this scale and position then the feature still remains significant at the 4.2σ level. The 5.3σ level translates into a fractional overdensity of 2.2. Checking with the published list of metal absorption lines compiled by Williger et al. (1996) we find at redshift 2.2722 CII, CIV, SiIV, and AlII absorption along just one of the sightlines (towards Q0041-2658). We have thus identified the presence of at least one galaxy (because of the heavy element absorption). We have also identified the existence of what appears to be a large cluster of Lyα absorbers, not only along the line of sight but also transverse to the line of sight at the same redshift as the galaxy. This is suggestive that Lyα clouds arise in the precursors of galaxy clusters and are therefore either galaxies themselves or reveal the presence of an intercluster medium.

There are also two prominent voids just below 4500 Å and at $\sim$ 4830 Å. The first void is flanked by two narrow, $\sim 3\sigma$ overdensities. We can see more detail in Figure 4 which shows another cross-section through the transmission surface at window size = 59 pixels which corresponds to $\sim 20\,h_{100}^{-1}$ comoving Mpc. The first void seems to be due to a rather prominent lack of absorption lines around 4480 Å in the spectrum of Q0041-2707 but it must be noted that it is not averaged out by the other *four* spectra which contribute to this region none of which (with perhaps the exception of Q0042-2656) show any strong absorption at this wavelength. The $\sim 3\sigma$ overdensity longward of this first void is caused by a coincident cluster of lines in the spectra Q0041-2638 and Q0042-2657. The separation between those two lines of sight is $6.4\,h_{100}^{-1}$ proper Mpc at redshift 2.77.

The case of the second void is more subtle. None of the four contributing spectra show any obvious lack of absorption lines and thus this void cannot be attributed to any particular spectrum. At the redshift of the void (2.97) the separations among this group of sightlines range from 3 to $6.4\,h_{100}^{-1}$ proper Mpc which is similar to the size of the window ($4.5\,h_{100}^{-1}$ proper Mpc). This void also manifests itself as the large blue patch at $\sim$ 4900 Å and window sizes of 200 to 400 pixels. However, this patch is *not* continued to the shortward side of the void. This asymmetry arises because there is no overdensity comparable to the one discussed before longward of the void. This void actually has its minimum at 4848 Å and at a size of just $2.3\,h_{100}^{-1}$ proper Mpc and is significant at the 4.1σ level. Again allowing for a 5 percent error in the continuum fit, the significance reduces to 3.0σ. The fractional underdensity implied by this feature is 0.38. However, on inspection of the positions and redshifts of the other quasars observed by Williger et al. we find that Q0042-2639 lies almost exactly in the middle of the quadrangle spanned by the four quasars used to calculate the transmission surface at the position of the void. Its redshift is given as 2.98 – just 750 km/s from the position of the void. At this redshift the distances to the sightlines of the other four quasars are (2.6, 2.6, 3.0, 3.8) h_{100}^{-1} proper Mpc. The 3000 km/s blueward of a quasar's emission redshift that were excluded from the analysis in order to avoid the proximity effect correspond to $3.8\,h_{100}^{-1}$ proper Mpc at this redshift. This strongly suggests that the lack of absorption is actually due to a "foreground proximity effect": the ultraviolet flux of the foreground quasar (Q0042-2639) increases the ionisation level of the surrounding hydrogen and thus depletes the neutral fraction of hydrogen that can contribute towards Lyα absorption in the spectra of the background quasars.

The ability to detect such "hidden" over- or underdensities is one of the more outstanding features of the tpdf analysis.

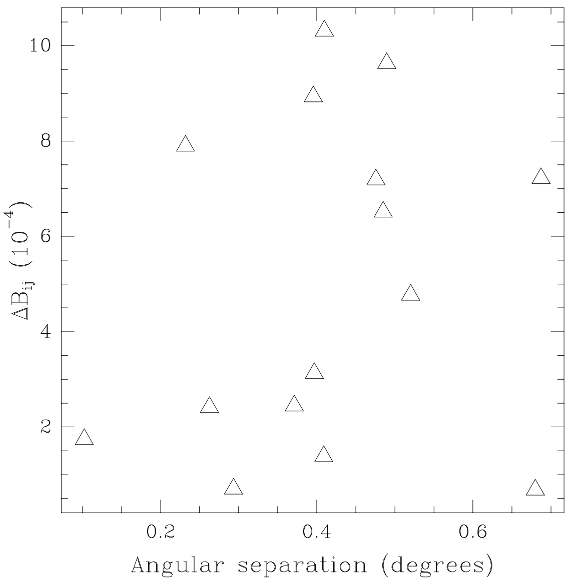

Fig. 1.— ΔB_{ij} vs. angular separation for six of the eight quasars.

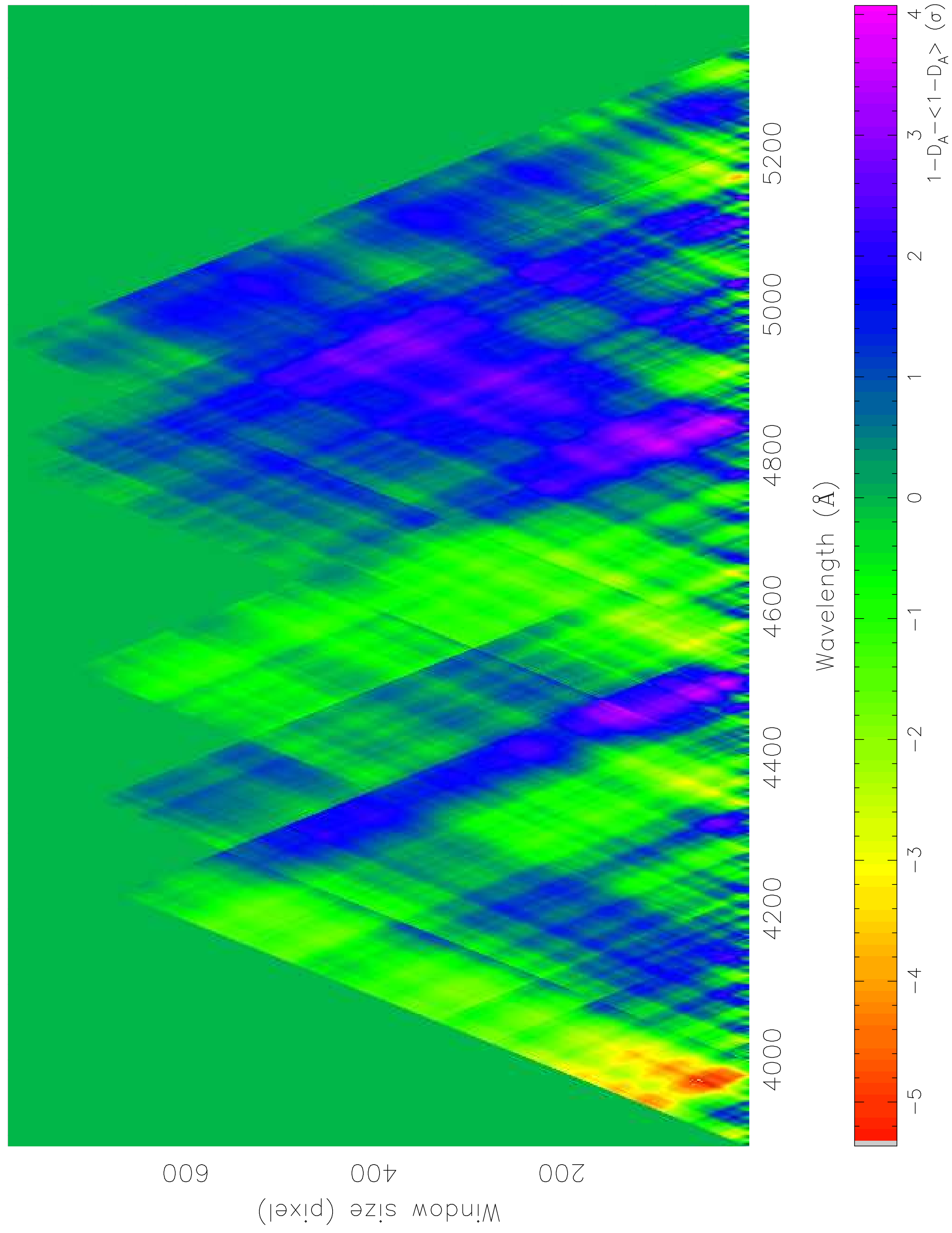

Fig. 2.— Transmission surface of Williger quasars.

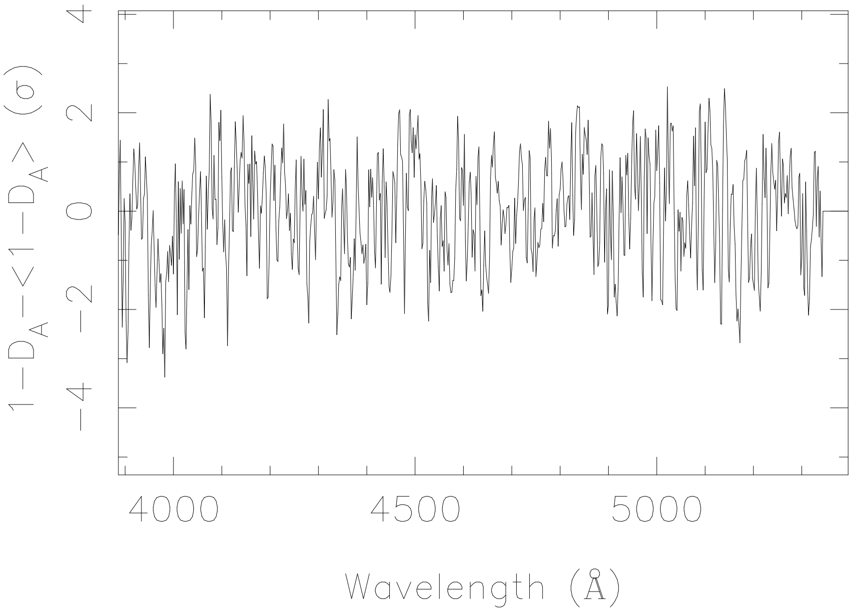

Fig. 3.— Cross-section through Figure 2 at window size = 1 pixel.

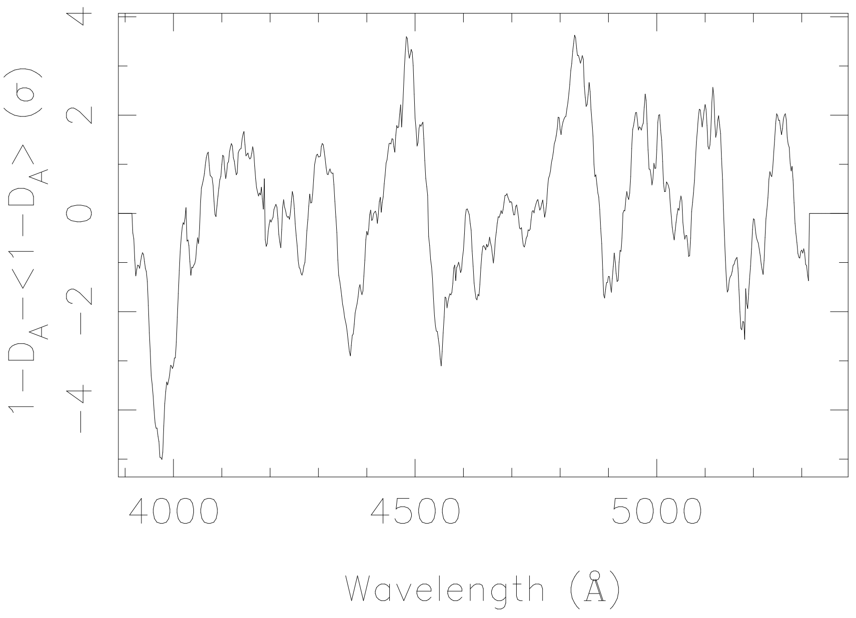

Fig. 4.— Cross-section through Figure 2 at window size = 59 pixels.

Chapter 7

Conclusions

Recent work (Lanzetta et al. 1995) at low redshift has shown that at least some fraction of the Lyα absorption lines seen in the spectra of high redshift quasars arises in the extended haloes of galaxies. At high redshift it has been found that Lyα absorbers are clustered (Fernández-Soto et al. 1996) and that many contain ionised carbon (Cowie et al. 1995). This suggests that high redshift Lyα absorbers may also be identified with the haloes of galaxies. Thus it seems likely that the Lyα forest may be used to study the large scale structure of the Universe.

However, the classical tool of cluster analysis, the two-point correlation function (Peebles 1993, Sargent et al. 1980), has revealed only very little clustering among the Lyα clouds and the question arises whether the two-point correlation function is the appropriate tool. Indeed, it has been shown (Liu & Jones 1990, Fernández-Soto et al. 1996) that significant clustering may be missed and the results presented in chapter 4 contribute to this evidence. There it was shown that both clusters of absorbers and sheet-like structures similar to the walls seen in the distribution of local galaxies remain undetected when employing the two-point correlation function. New methods of analysis are called for and some have already been successfully applied (Pando & Fang 1996, Zuo & Bond 1994).

In this work I have presented a new technique to search for non-randomness in the spatial distribution of the Lyα forest based on the first and second moments of the transmission probability density function. This method is able to identify the strength, position and scale of individual structures since it retains spatial information. It is fairly insensitive to noise and resolution characteristics and is easy to apply in practice. The technique has been tested with the help of synthetic spectra which are produced by simulating the spatial distribution of absorbing galaxies. By employing different clustering models the capability of the new analysis to recover large structures from the spectra has been assessed and its sensitivity was found to be adequate.

The method was applied to the spectra of a close group of eight quasars with a mean redshift of 2.97. At least two significant large scale features have been detected at the 5 and 4σ level:

1. An overdense structure (5.3σ) of size $\sim 6.8\, h_{100}^{-1}$ proper Mpc in the line of sight direction and probably at least $2.4\, h_{100}^{-1}$ proper Mpc in the plane of the sky. This feature remains significant at the 4.2σ level if one allows for a 5 percent error in the continuum. The fractional overdensity of this structure is 2.2 and metal absorption lines have been found at almost exactly the same redshift. A cluster or proto-cluster of galaxies therefore appears to have been discovered at redshift 2.27. This result supports the evidence that the Lyα forest traces large scale structure.

2. A void of dimensions $\sim 4.5\, h_{100}^{-1}$ proper Mpc (line of sight) $\times$ $(3 - 6.4)\, h_{100}^{-1}$ proper Mpc (plane of sky) at redshift 2.97. This underdensity is significant at the 4.1σ level, reduced to 3.0σ when allowing for a 5 percent error in the continuum fit. It may be caused by a locally increased UV ionising flux due to a foreground quasar lying relatively close to the sightlines towards the background quasars. This foreground quasar lies within 750 km/s of the void.

Future work

The simulations presented in chapter 3 form the basis for a more realistic three dimensional model of the Universe incorporating detailed physical information such as e.g. the number counts as a function of galaxy type or the morphology and kinematics of halo gas in different types of galaxies. In addition, other clustering models and their effect on Lyα forest spectra will be explored.

The possibilities of tpdf analyses with respect to clustering have so far not been fully explored. Because of the intrinsic asymmetry of the tpdf it is likely that the 3rd moment, or skew, of the tpdf is a very sensitive tool for analysing the Lyα forest. In order to be able to *measure* the 2nd and 3rd moments of the tpdf accurately one needs a very large sample of high quality spectra. The advent of the "2 degree field" (2df) multifibre spectrograph will hopefully make such data sets available soon.

It is also conceivable that better results might be obtained by the use of e.g. a Gaussian instead of a top-hat function with which to convolve the spectra. The top-hat function was used for purely historical reasons, i.e. because of its connection with the well established quantity D_A. In practice, any function could be used that does not unduly complicate the calculations presented in section 2.3. If overdensities in the redshift distribution of absorbers were Gaussian (as would be expected for small scale overdensities due to the approximately Gaussian distribution of peculiar velocities) then the use of a Gaussian as a convolving function would be more effective than a top-hat function. Also, a top-hat function has power on all scales in Fourier space and thus the analysis remains sensitive to small scale power (through the side lobes) when investigating large scales.

If future work confirms the hypothesis that the Lyα forest *does* reliably trace large scale structure then the kind of analysis presented in this work will help in directly measuring the power spectrum of the primordial density fluctuations and thus constrain cosmological models.

Finally, the foreground proximity effect result described above will yield an estimate of the UV background flux at high redshift.

Appendix A

If two objects, A and B, are at the same cosmological distance corresponding to redshift z, but object B is moving with respect to object A at a velocity v, what is the redshift of object B? Imagine both objects emitting a photon of wavelength λ_0. At the moment of emission, the photon from object B is already Doppler-shifted according to the well known special relativistic formula:

$$\lambda_0' = \lambda_0 \sqrt{\frac{1+\beta}{1-\beta}}, \tag{A.1}$$

where $\beta = v/c$. As the photons travel on to the observer they are both redshifted by the expansion of he Universe. The photons from object A and B are measured at

$$\lambda_{\rm obs} = \lambda_0(1+z) \tag{A.2}$$

and

$$\lambda_{\rm obs}' = \lambda_0'(1+z) \tag{A.3}$$

respectively. Thus we have for the redshift of object B:

$$1+z' = \frac{\lambda_{\rm obs}'}{\lambda_0} = \frac{\lambda_0'(1+z)}{\lambda_0} = (1+z)\sqrt{\frac{1+\beta}{1-\beta}}. \tag{A.4}$$

Finally, we arrive at

$$\beta = \frac{(1+z')^2-(1+z)^2}{(1+z')^2+(1+z)^2}. \tag{A.5}$$

For small β we have $\sqrt{\frac{1+\beta}{1-\beta}} \approx 1+\beta$ and therefore

$$\beta = \frac{\Delta z}{1+z}. \tag{A.6}$$

Bibliography

Bechtold, J., Green, R. F., Weymann, R. J., Schmidt, M., Estabrook, F. B., Sherman, R. D., and Wahlquist, H. D., 1984, *Astrophys. J.* **281**, 76

Bond, J. R. and Wadsley, J. W., 1997, preprint, astro-ph/9703125

Broadhurst, T. J., Ellis, R. S., Koo, D., and Szalay, A. S., 1990, *Nature* **343**, 726

Carswell, R. F., Morton, D. C., Smith, M. G., Stockton, A. N., Turnshek, D. A., and Weymann, R. J., 1984, *Astrophys. J.* **278**, 486

Carswell, R. F., Webb, J. K., Baldwin, J. A., and Atwood, B., 1987, *Astrophys. J.* **319**, 709

Cen, R. and Simcoe, R. A., 1997, *Astrophys. J.* in press

Charlton, J. C., Churchill, C. W., and Linder, S. M., 1995, *Astrophys. J., Lett.* **452**, L81

Connolly, A. J., Szalay, A. S., Romer, A. K., Nichol, R., Holden, B., Koo, D., and Miyaji, T., 1997, preprint, astro-ph/9702025

Cooke, A. J., Espey, B., and Carswell, R. F., 1997, *Mon. Not. R. Astron. Soc.* **284**, 552

Cowie, L. L., Songaila, A., Kim, T.-S., and Hu, E. M., 1995, *Astron. J.* **109**, 1522

Cristiani, S., 1995, Lecture, astro-ph/9512086

Crotts, A. P. S. and Fang, Y., 1997, *Astrophys. J.* submitted, astro-ph/9702185

Di Nella, H., Couch, W. J., Paturel, G., and Parker, Q. A., 1996, *Mon. Not. R. Astron. Soc.* **283**, 367

Dinshaw, N., Impey, C. D., Foltz, C. B., Weyman, R. J., and Chaffee, F. H., 1994, *Astrophys. J., Lett.* **437**, L87

Drinkwater, M., 1987, *Ph.D. thesis*, University of Cambridge

Einasto, J., Einasto, M., Gottlöber, S., Müller, V., Saar, V., Starobinsky, A. A., Tago, E., Tucker, D., Andernach, H., and Frisch, P., 1997, *Nature*, accepted, astro-ph/9701018

Ettori, S., Guzzo, L., and Tarenghi, M., 1997, *Mon. Not. R. Astron. Soc.* **285**, 218

Fadda, D., Girardi, M., Giuricin, G., Mardirossian, F., and Mezzetti, M., 1996, *Astrophys. J.* **473**, 670

Fernández-Soto, A., Lanzetta, K. M., Barcons, X., Carswell, R. F., and Webb, J. K., 1996, *Astrophys. J., Lett.* **460**, L85

Hernquist, L., Katz, N., Weinberg, D. H., and Miralda-Escudé, J., 1996, *Astrophys. J., Lett.* **457**, L51

Hu, E. M., Kim, T.-S., Cowie, L. L., Songaila, A., and Rauch, M., 1995, *Astron. J.* **110**, 1526

Jenkins, E. B. and Ostriker, J. P., 1991, *Astrophys. J.* **376**, 33

Jenkins, G. M. and Watts, D. G., 1968, *Spectral Analysis and its Applications*, Holden-Day, San Francisco

Khare, P., Srianand, R., York, D. G., Green, R., Welty, D., Huang, K.-L., and Bechtold, J., 1997, *Mon. Not. R. Astron. Soc.* **285**, 167

King, I. R., 1966, *Astron. J.* **71**, 64

Kirkman, D. and Tytler, D., 1997, preprint, astro-ph/9701209

Lang, K. R., 1980, *Astrophysical Formulae*, Springer-Verlag, Berlin

Lanzetta, K. M., Bowen, D. B., Tytler, D., and Webb, J. K., 1995, *Astrophys. J.* **442**, 538

Liu, X. D. and Jones, B. J. T., 1990, *Mon. Not. R. Astron. Soc.* **242**, 678

Lu, L., Sargent, W. L. W., Womble, D. S., and Takada-Hidai, M., 1996, *Astrophys. J.* **472**, 509

Lu, L. and Zuo, L., 1994, *Astrophys. J.* **426**, 502

Lynds, R., 1971, *Astrophys. J., Lett.* **164**, L73

Miralda-Escudé, J., Cen, R., Ostriker, J. P., and Rauch, M., 1996, *Astrophys. J.* **471**, 582

Misner, C. W., Thorne, K. S., and Wheeler, J. A., 1973, *Gravitation*, W. H. Freeman and Company, San Francisco

Natarajan, P., 1996, private communication

Neyman, J. and Scott, E. L., 1952, *Astrophys. J.* **116**, 144

O'Brien, P. T., Gondhalekar, P. M., and Wilson, R., 1988, *Mon. Not. R. Astron.*

Soc. **233**, 801

Oke, J. B. and Korycansky, D. G., 1982, *Astrophys. J.* **255**, 11

Pando, J. and Fang, L.-Z., 1996, *Astrophys. J.* **459**, 1

Peebles, P. J. E., 1993, *Principles of Physical Cosmology*, Princeton University Press, Princeton, New Jersey

Petitjean, P., Webb, J. K., Rauch, M., Carswell, R. F., and Lanzetta, K., 1993, *Mon. Not. R. Astron. Soc.* **262**, 499

Press, William, H. and Rybicki, G. B., 1993, *Astrophys. J.* **418**, 585

Press, William, H., Rybicki, G. B., and Schneider, D. P., 1993, *Astrophys. J.* **414**, 64

Quashnock, J. M., Vanden Berk, D. E., and York, D. G., 1997, *Astrophys. J., Lett.* **472**, L69

Rauch, M., Carswell, R. F., Chaffee, F. H., Foltz, C. B., Webb, J. K., Weymann, R. J., Bechtold, J., and Green, R. F., 1992, *Astrophys. J.* **390**, 387

Rauch, M., Miralda-Escudé, J., Sargent, W. L. W., Barlow, T. A., Weinberg, D. H., Hernquist, L., Katz, N., Cen, R., and Ostriker, J. P., 1997, *Astrophys. J.* submitted

Sargent, W. L. W., Young, P., and Schneider, D. P., 1982, *Astrophys. J.* **256**, 374

Sargent, W. L. W., Young, P. J., Boksenberg, A., and Tytler, D., 1980, *Astrophys. J., Suppl. Ser.* **42**, 41

Saslaw, W. C., 1989, *Astrophys. J.* **341**, 588

Saslaw, W. C., 1992, *Astrophys. J.* **391**, 423

Saslaw, W. C. and Hamilton, A. J. S., 1984, *Astrophys. J.* **276**, 13

Sheth, R. K. and Saslaw, W. C., 1994, *Astrophys. J.* **437**, 35

Steidel, C. C. and Sargent, W. L. W., 1987, *Astrophys. J.* **313**, 171

Ulmer, A., 1996, *Astrophys. J.* **473**, 110

van de Weygaert, R., 1991, *Ph.D. thesis*, Rijksuniversiteit te Leiden

Webb, J. K., 1987, in A. Hewitt, G. Burbidge, and L.-Z. Fang (eds.), *Observational Cosmology*, p. 803

Webb, J. K., 1996, private communication

Webb, J. K., Barcons, X., Carswell, R. F., and Parnell, H. C., 1992, *Mon. Not. R. Astron. Soc.* **255**, 319

Webb, J. K. and Hetem, A., 1993, private communication

Webb, J. K. and Larsen, I. P., 1987, in J. Bergeron (ed.), *Proceedings of 3rd IAP workshop, "Primeval and High Redshift Galaxies"*, p. 419

Weymann, R. J., Carswell, R. F., and Smith, M. G., 1981, *Ann. Rev. Astron. Astrophys.* **19**, 41

Williger, G. M., Baldwin, J. A., Carswell, R. F., Cooke, A. J., Hazard, C., Irwin, M. J., McMahon, R. G., and Storrie-Lombardi, L. J., 1994, *Astrophys. J.* **428**, 574

Williger, G. M., Hazard, C., Baldwin, J. A., and McMahon, R. G., 1996, *Astrophys. J., Suppl. Ser.* **104**, 145

Williger, G. M., Smette, A., Hazard, C., Baldwin, J. A., and McMahon, R. G., 1997, *Nature* submitted

Zhang, Y., Anninos, P., and Norman, M. L., 1995, *Astrophys. J., Lett.* **453**, L57

Zuo, L., 1993, *Astron. Astrophys.* **278**, 343

Zuo, L. and Bond, J. R., 1994, *Astrophys. J.* **423**, 73

Zuo, L. and Lu, L., 1993, *Astrophys. J.* **418**, 601

Zuo, L. and Phinney, E. S., 1993, *Astrophys. J.* **418**, 28

Acknowledgments

Many people have helped and encouraged me during this past year. In particular, I would like to thank my supervisor John Webb for being a great and inspiring teacher and for always finding the time to answer my endless questions. Thank you also to Prof. Mebold for supporting this collaboration with the University of New South Wales. I am grateful to Bob Carswell for hosting me at the Institute of Astronomy for the first three months of this work and for helping me to find my feet.

I am indebted to Gerard Williger and his collaborators for making their excellent data available to me.

A special thanks goes to Ed Salpeter and Andrew Liddle for many interesting discussions and helpful comments.

I would also like to thank everyone in the Department of Astrophysics and Optics at UNSW (especially room 136) for their friendship and support.

Last but not least, I want to thank my parents for believing in me and making it all possible in the first place.

Ich versichere, daß ich diese Arbeit selbständig verfaßt und keine anderen als die angegebenen Quellen und Hilfsmittel benutzt sowie Zitate kenntlich gemacht habe.